J. Fluid Mech. (2018), *vol.* 847, *pp.* 386–416.
doi:10.1017/jfm.2018.305

Swimming performance, resonance and shape evolution in heaving flexible panels

Alexander P. Hoover[1,†], Ricardo Cortez[1], Eric D. Tytell[2] and Lisa J. Fauci[1]

[1]Department of Mathematics, Tulane University, New Orleans, LA 70118, USA

[2]Department of Biology, Tufts University, Medford, MA 02155, USA

(Received 1 May 2017; revised 26 February 2018; accepted 4 April 2018;
first published online 23 May 2018)

Many animals that swim or fly use their body to accelerate the fluid around them, transferring momentum from their flexible bodies and appendages to the surrounding fluid. The kinematics that emerge from this transfer result from the coupling between the fluid and the active and passive material properties of the flexible body or appendages. To elucidate the fundamental features of the elastohydrodynamics of flexible appendages, recent physical experiments have quantified the propulsive performance of flexible panels that are actuated on their leading edge. Here we present a complementary computational study of a three-dimensional flexible panel that is heaved sinusoidally at its leading edge in an incompressible, viscous fluid. These high-fidelity numerical simulations enable us to examine how propulsive performance depends on mechanical resonance, fluid forces, and the emergent panel deformations. Moreover, the computational model does not require the tethering of the panel. We therefore compare the thrust production of tethered panels to the forward swimming speed of the same panels that can move forward freely. Varying both the passive material properties and the heaving frequency of the panel, we find that local peaks in trailing edge amplitude and forward swimming speed coincide and that they are determined by a non-dimensional quantity, the effective flexibility, that arises naturally in the Euler–Bernoulli beam equation. Modal decompositions of panel deflections reveal that the amplitude of each mode is related to the effective flexibility. Panels of different material properties that are actuated so that their effective flexibilities are closely matched have modal contributions that evolve similarly over the phase of the heaving cycle, leading to similar vortex structures in their wakes and comparable thrust forces and swimming speeds. Moreover, local peaks in the swimming speed and trailing edge amplitude correspond to peaks in the contributions of the different modes. This computational study of freely swimming flexible panels gives further insight into the role of resonance in swimming performance that is important in the engineering and design of robotic propulsors. Moreover, we view this reduced model and its comparison to laboratory experiments as a building block and validation for a more comprehensive three-dimensional computational model of an undulatory swimmer that will couple neural activation, muscle mechanics and body elasticity with the surrounding viscous, incompressible fluid.

Key words: biological fluid dynamics, propulsion, swimming/flying

† Email address for correspondence: ahoover2@tulane.edu

1. Introduction

The impact of flexibility on propulsion has been the focus of research in many different biological systems, such as swimming jellyfish (Demont & Gosline 1988; Megill, Gosline & Blake 2005; Colin *et al.* 2012; Hoover & Miller 2015; Hoover, Griffith & Miller 2017), swimming lamprey (Tytell *et al.* 2010; Tytell, Hsu & Fauci 2014; Hamlet, Fauci & Tytell 2015; Tytell *et al.* 2016) and flying insects (Miller & Peskin 2009). In addition, Leftwich *et al.* (2012) examined the effect of a flexible tail on the swimming performance of a robotic lamprey. Other studies use simplified physical models, where a flexible hydrofoil or panel takes the place of an animal's flexible appendage (Alben *et al.* 2012; Dewey *et al.* 2013; Paraz, Eloy & Schouveiler 2014). Most of these studies analyse the propulsive performance of a tethered panel whose leading edge is driven in a periodic motion in a flow tank (Dewey *et al.* 2013). In these studies, the experimental set-up is adjusted to examine the effects of many different factors, such as the elastic properties of the panel (Quinn, Lauder & Smits 2014*b*; Lucas *et al.* 2015), panel geometries (Buchholz & Smits 2006, 2008; Green, Rowley & Smits 2011), the motion of the leading edge (Hover, Haugsdal & Triantafyllou 2004; Licht *et al.* 2010; Lehn *et al.* 2017) and wall effects (Quinn, Lauder & Smits 2014*a*, 2015). Other simplified models examine the hydrodynamics of free-swimming panels with flexibility localized to a torsional spring present at the leading edge (Alben & Shelley 2005; Vandenberghe, Childress & Zhang 2006; Spagnolie *et al.* 2010; Ramananarivo, Godoy-Diana & Thiria 2011).

The motivation of many of these studies has been the potential benefits of biomimetics in engineering. Recent advances in biologically inspired underwater vehicles have given an impetus to understanding the role of flexibility in enhancing their swimming performance (Colin *et al.* 2012; Raj & Thakur 2016). For vehicles that are propelled with the actuation of flexible propulsors, understanding the role of mechanical resonance can yield insight into design of the vehicle and an optimized pattern of actuation (Chu *et al.* 2012). By examining these problems from a modelling perspective, we can shed light on the limitations and constraints that have shaped biological organisms and how these can inform future vehicle design (Fish & Beneski 2014).

In addition to physical models, computational models have been developed to investigate the fluid mechanics of flapping propulsion. In many cases, the role of flexibility in propulsion is not considered fully and the kinematics of the swimmer is prescribed (Dong, Mittal & Najjar 2006; Borazjani & Sotiropoulos 2008, 2009). Other studies account for the flexibility of the panels in the motion of the leading edge, but not the body itself (Eldredge, Toomey & Medina 2010; Spagnolie *et al.* 2010; Moore 2014, 2015). Models that employ inviscid fluid assumptions must take steps to account for vorticity generated by the fluid–structure interface (Liu & Bose 1997; Alben 2008; Michelin & Llewellyn Smith 2009; Alben *et al.* 2012; Moore 2017). A model of lamprey locomotion that does capture the full elastohydrodynamic coupling in a Navier–Stokes fluid (Tytell *et al.* 2010) actuated by detailed muscle mechanics (Hamlet *et al.* 2015) has been used to explore the role of flexibility in swimming performance, but only in a two-dimensional domain. While two-dimensional models do capture many features of the three-dimensional system (de Sousa & Allen 2011; Shoele & Zhu 2012; Zhu, He & Zhang 2014; Tytell *et al.* 2016; Andersen *et al.* 2017), the spatio-temporal evolution of the vortex structures in the wake of a swimmer or a flapping panel are affected by the spanwise geometry of the panel (Buchholz & Smits 2006, 2008; Green & Smits 2008; Green *et al.* 2011; Van Buren *et al.* 2017).

Several of these recent studies have focused on the role of the effective flexibility, a quantity that describes the ratio of inertial added mass forces from the fluid to the internal bending forces of the panel, derived from the Euler–Bernoulli beam equation. The experiments of Quinn *et al.* (2014*b*) demonstrated that resonant peaks in thrust production and trailing edge amplitude were realized at certain effective flexibilities. It was also suggested that these correspond to peaks in the modal contributions of different beam modes. Additionally Lucas *et al.* (2014) observed that flexible appendages of different animals deform in a similar manner during swimming and flying strokes, suggesting the presence of bending laws for enhanced thrust production that transcend the fluid medium, animal size and phylogenetic background.

With these unifying principles in mind, we present a three-dimensional computational elastohydrodynamic model of a flexible panel in a fluid described by the Navier–Stokes equations. We investigate the connection between Euler–Bernoulli beam modes, the evolving kinematics of the panel over the heaving cycle and the vortex structures generated in the fluid. In our immersed boundary framework, the leading edge of the panel is heaved in a sinusoidal manner and the resulting panel deformation is a result of the interplay between the panel's internal bending forces and the inertial forces from the fluid. We compute the resulting thrust of tethered panels due to a heaving actuation as well as the swimming speeds of untethered panels that are free to move forward. For panels with different heaving frequencies and bending moduli, we measure propulsive performance as a function of the non-dimensional effective flexibility of the system. To understand the evolution of panel deformation, beam mode analysis is performed. We find that panels of different material properties that are actuated so that their effective flexibilities are closely matched have modal contributions that evolve similarly over the phase of the heaving cycle, resulting in similar thrust forces, amplitudes and swimming speeds. We also find that the wakes behind panels in simulations where effective flexibilities are matched exhibit strong agreement in dominant vortex structures generated by the panel deflections over the heaving cycle.

While quantifying the role of resonance in the swimming performance of flapping, flexible panels is of intrinsic value, we also view the computational study presented here and its comparison to previous laboratory experiments as a major step towards a more comprehensive three-dimensional computational model of an undulatory swimmer that will couple neural activation, muscle mechanics and body elasticity in a Navier–Stokes fluid.

2. Materials and methods

2.1. *Fluid–structure interaction*

Fluid–structure interaction problems are common to biological systems and have been examined with a variety of computational frameworks. The immersed boundary (IB) method (Peskin 2002; Mittal & Iaccarino 2005) is an approach to fluid–structure interaction introduced by Peskin to study blood flow in the heart (Peskin 1977). The IB method has been used to model the fluid dynamics of animal locomotion in the low to intermediate Reynolds number regime, including undulatory swimming (Fauci & Peskin 1988; Bhalla *et al.* 2013), insect flight (Miller & Peskin 2004, 2005, 2009; Jones *et al.* 2015), lamprey swimming (Tytell *et al.* 2010; Hamlet *et al.* 2015; Tytell *et al.* 2016), crustacean swimming (Zhang *et al.* 2014) and jellyfish swimming (Hamlet, Santhanakrishnan & Miller 2011; Herschlag & Miller 2011; Hoover & Miller 2015; Hoover *et al.* 2017).

The IB formulation of fluid–structure interaction uses an Eulerian description of the momentum and incompressibility equations of the coupled fluid–structure system, and it uses a Lagrangian description of the structural deformations and stresses. Here $\boldsymbol{x} = (x, y, z) \in \Omega$ denotes physical Cartesian coordinates, where Ω is the physical region occupied by the fluid–structure system. Let $\boldsymbol{X} = (X, Y, Z) \in U$ denote Lagrangian material coordinates that are attached to the structure, with U denoting the Lagrangian coordinate domain. The Lagrangian material coordinates are mapped to the physical position of material point $\boldsymbol{X}$ at time t by $\boldsymbol{\chi}(\boldsymbol{X}, t) = (\chi_x(\boldsymbol{X}, t), \chi_y(\boldsymbol{X}, t), \chi_z(\boldsymbol{X}, t)) \in \Omega$, so that the physical region occupied by the structure at time t is $\boldsymbol{\chi}(U, t) \subset \Omega$.

The immersed boundary formulation of the coupled system is

$$\rho\left(\frac{\partial \boldsymbol{u}(\boldsymbol{x}, t)}{\partial t} + \boldsymbol{u}(\boldsymbol{x}, t) \cdot \nabla \boldsymbol{u}(\boldsymbol{x}, t)\right) = -\nabla p(\boldsymbol{x}, t) + \mu \nabla^2 \boldsymbol{u}(\boldsymbol{x}, t) + \boldsymbol{f}(\boldsymbol{x}, t), \tag{2.1}$$

$$\nabla \cdot \boldsymbol{u}(\boldsymbol{x}, t) = 0, \tag{2.2}$$

$$\boldsymbol{f}(\boldsymbol{x}, t) = \int_U \boldsymbol{F}(\boldsymbol{X}, t)\, \delta(\boldsymbol{x} - \boldsymbol{\chi}(\boldsymbol{X}, t))\, \mathrm{d}\boldsymbol{X}, \tag{2.3}$$

$$\int_U \boldsymbol{F}(\boldsymbol{X}, t) \cdot \boldsymbol{V}(\boldsymbol{X})\, \mathrm{d}\boldsymbol{X} = -\int_U \boldsymbol{P}(\boldsymbol{X}, t) : \nabla_{\boldsymbol{X}} \boldsymbol{V}(\boldsymbol{X})\, \mathrm{d}\boldsymbol{X} + \int_U \boldsymbol{G}(\boldsymbol{X}, t) \cdot \boldsymbol{V}\, \mathrm{d}\boldsymbol{X}, \tag{2.4}$$

$$\frac{\partial \boldsymbol{\chi}(\boldsymbol{X}, t)}{\partial t} = \int_\Omega \boldsymbol{u}(\boldsymbol{x}, t)\, \delta(\boldsymbol{x} - \boldsymbol{\chi}(\boldsymbol{X}, t))\, \mathrm{d}\boldsymbol{x}. \tag{2.5}$$

Here ρ is the fluid density of water (1000 kg m^{-3}), μ is the dynamic viscosity of water (0.001 N s m^{-2}), $\boldsymbol{u}(\boldsymbol{x}, t) = (u_x, u_y, u_z)$ is the Eulerian material velocity field and $p(\boldsymbol{x}, t)$ is the Eulerian pressure. Another quantity of interest is vorticity, $\nabla \times \boldsymbol{u} = \boldsymbol{\omega} = (\omega_x, \omega_y, \omega_z)$. Here, $\boldsymbol{f}(\boldsymbol{x}, t)$ and $\boldsymbol{F}(\boldsymbol{X}, t)$ are Eulerian and Lagrangian force densities. $\boldsymbol{F}$ is defined in terms of the first Piola–Kirchhoff solid stress tensor, $\boldsymbol{P}$, in (2.4) and an external force acting on the body, $\boldsymbol{G}(\boldsymbol{X}, t)$, using a weak formulation, in which $\boldsymbol{V}(\boldsymbol{X})$ is an arbitrary Lagrangian test function. In this study, the panel is neutrally buoyant. The Eulerian and Lagrangian frames are connected using the Dirac delta function $\delta(\boldsymbol{x})$ as the kernel of the integral transforms of (2.3) and (2.5).

A hybrid finite difference/finite element version of the immersed boundary method is used to approximate equations (2.1)–(2.5). This IB/FE method uses a finite difference formulation for the Eulerian equations and a finite element formulation to describe the flexible panel body. More details on the IB/FE method can be found in Griffith & Luo (2016).

2.2. *Material model*

The structural model of the panel accounts for its passive elastic properties as well as a body force that heaves the panel at its leading edge. Throughout this study, the panel geometry will maintain a fixed span (s), chord length (c) and thickness (w). The structural stresses due to the passive elastic properties of the panel are calculated using the first Piola–Kirchhoff stress tensor of a neo-Hookean material model

$$\boldsymbol{P} = \eta \mathbb{F} + (\lambda \log(J) - \eta)\mathbb{F}^{-T}, \tag{2.6}$$

where $\mathbb{F} = \partial \boldsymbol{\chi} / \partial \boldsymbol{X}$ is the deformation gradient of the mesh, J is the Jacobian of $\mathbb{F}$, η is the shear modulus and λ is the bulk modulus. The shear and bulk moduli are defined respectively as

$$\eta = \frac{E}{2(1 + \nu)} \tag{2.7}$$

Chord length	c	0.05 m
Span length	s	0.03 m
Panel thickness	w	0.001 m
Heaving amplitude	a	0.005 m
Poisson ratio	ν	0.3
Bending modulus	EI	1×10^{-6}, 5×10^{-7}, 1×10^{-7}, 5×10^{-8} and 1×10^{-8} N m^2
Target point strength	κ	1×10^{10} N m^{-1}

TABLE 1. Table of model parameters.

and

$$\lambda = \frac{E\nu}{(1+\nu)(1-2\nu)}, \tag{2.8}$$

where E is Young's modulus (N m^{-2}) and ν is the Poisson ratio. The bending modulus of a rectangular panel is defined as

$$EI = \frac{Esw^3}{12(1-\nu^2)}, \tag{2.9}$$

where I is the second moment of area of the panel. Note that the neo-Hookean material model of (2.6) has a nonlinear stress–strain relationship, although it is approximately linear for small deformations (Bonet & Wood 1997). Here EI is set as an input for our material model. Over the following set of simulations, five panel rigidities (see table 1) are selected.

The heaving motion of the panel is actuated with an external force $\boldsymbol{G}(\boldsymbol{X}, t)$ on the leading edge of the panel. This time-dependent external force may be thought of as arising from stiff tether springs between material points on the panel's leading edge and virtual points that follow a prescribed motion:

$$\boldsymbol{G}(\boldsymbol{X}, t) = \begin{cases} \kappa(\boldsymbol{\chi}_T(\boldsymbol{X}, t) - \boldsymbol{\chi}(\boldsymbol{X}, t)) & \text{if } \boldsymbol{X} \in U_{LE}, \\ 0 & \text{if } \boldsymbol{X} \notin U_{LE}, \end{cases} \tag{2.10}$$

where κ is a spring constant and $\boldsymbol{\chi}_T(\boldsymbol{X}, t)$ is the desired position of $\boldsymbol{X}$ at time t. Here $U_{LE} \subset U$ represents the portion of the panel where the external force is applied, which is the leading edge of the panel and is 2 % of the panel length. The desired position of the leading edge of tethered panels is

$$\boldsymbol{\chi}_T(\boldsymbol{X}, t) = \left(\chi_x(\boldsymbol{X}, 0),\, \chi_y(\boldsymbol{X}, 0),\, \chi_z(\boldsymbol{X}, 0) + \frac{a}{2}\sin(2\pi\phi t)\right), \tag{2.11}$$

so that the leading edge is constrained in all three dimensions to move only along the z-direction. The untethered panels are unconstrained in the swimming direction, so for this case we modify the first component of $\boldsymbol{\chi}_T$ to be $\chi_x(\boldsymbol{X}, t)$, which effectively eliminates any external force in the x-direction. We point out that the elastic forces from the material model are fully three-dimensional. In both the tethered and untethered cases, no background flow is imposed.

2.3. *Beam mode analysis*

The one-dimensional Euler–Bernoulli beam equation that approximates the deflections H of a flexible panel due to an external force is

$$\rho_p sw\frac{\partial^2 H}{\partial T^2} + EI\frac{\partial^4 H}{\partial X^4} = F_{ext}, \tag{2.12}$$

where ρ_p is the density of the panel and F_{ext} is the external force per unit length. While the elastohydrodynamic system of the flapping flexible panel in a viscous, incompressible fluid is not fully captured by this equation, its analysis does allow one to identify an important non-dimensional parameter that governs the dynamics and gives insight into the evolving panel kinematics (Paraz *et al.* 2014; Quinn *et al.* 2014*b*, 2015).

Assuming $\rho_p/\rho = O(1)$ and $w/s \ll 1$, the inertia from the panel is dominated by the added mass forces from the fluid, and $\rho_p ws$ is replaced by an effective mass per unit length, ρsc. Defining the dimensionless small parameter $\epsilon^2 = \rho_p w/\rho c$ and using the scalings $X^* = X/c$, $H^* = H/a$, $T^* = T\phi/\epsilon$ and $F^*_{ext} = (c^4/aEI)F_{ext}$, the beam equation becomes

$$\Pi^2\frac{\partial^2 H^*}{\partial T^{*2}} + \frac{\partial^4 H^*}{\partial X^{*4}} = F^*_{ext}, \tag{2.13}$$

where

$$\Pi = \sqrt{\frac{\rho sc^5\phi^2}{EI}}. \tag{2.14}$$

Here Π is a non-dimensional parameter known as the effective flexibility, and $\mathcal{F}^*_{ext} \equiv \mathcal{F}_{ext}c^4/(EIa)$. The effective flexibility is the ratio of added mass forces from the fluid to the internal bending forces of the elastic panel.

For the boundary conditions $H^*(0, T^*) = 0$ and $H^{*'}(0, T^*) = 0$ and $H^{*''}(1, T^*) = 0$ and $H^{*'''}(1, T^*) = 0$ one can compute the orthonormal eigenfunctions Ψ_i of (2.13) (Weaver, Timoshenko & Young 1990). This is a natural basis to expand the evolving panel shapes from the computational model. By choosing a cross-section down the middle of the panel and averaging over its thickness, we can describe the panel deflections by $H^*_{sim}(X^*, T^*)$. For each time T^*, we can write $H^*_{sim}(X^*, T^*) = \sum_{i=1}^{\infty}\Psi_i(X^*)\Theta_i(T^*)$, where Ψ_i are orthonormal eigenfunctions and the Θ_i are their modal contributions. The modal contributions of each eigenfunction are found by taking the inner product of H^*_{sim} with each eigenfunction,

$$\Theta_i(T^*) = \int_0^1 H^*_{sim}(X^*, T^*)\Psi_i(X^*)\,\mathrm{d}X^* \tag{2.15}$$

over the length of the panel. Again, H^*_{sim} represents the vertical deflection of the panel resulting from the fluid–structure system. This modal decomposition allows us to separate the deflections of our panel into the sum of the modal contributions of each eigenfunction. At every time step, the panel's first five modal contributions (Θ_i, $i = 1, 2, 3, 4, 5$) are recorded.

To understand whether two panels had a similar evolution over the phase of the heaving cycle, we treated the modal contributions of each panel as signals for which we could measure the correlation between pairs. Here the modal contribution correlation of two panels of differing effective flexibilities, panel p and panel q, is defined as

$$\boldsymbol{C}_i^{pq} = \frac{1}{N-1}\sum_{n=1}^{N}\frac{\Theta_i^p(\xi_n) - \mu_i^p}{\sigma_i^p}\frac{\Theta_i^q(\xi_n) - \mu_i^q}{\sigma_i^q}, \tag{2.16}$$

where Θ_i^p and Θ_i^q are the ith modal contributions of panel p and panel q, μ_i^p and σ_i^p are the mean and standard deviation of Θ_i^p, μ_i^q and σ_i^q are the mean and standard deviation of Θ_i^q, ξ_n represents the time points of the phase collected over N observations. Here $\boldsymbol{C}_i^{pq}$ represents the pq entry of the correlation matrix, $\boldsymbol{C}_i \in \mathbb{R}^{120\times 120}$. Due to differences in the length of the heaving cycle, the modal contributions are interpolated so as to be compared at the same time points of the phase.

Modal contributions do not significantly contribute to the deflection of the panel if their amplitudes are small. Therefore, we weighted the correlations by the mode amplitudes and normalized by the maximum modal contribution of all panels, as follows:

$$Q^{pq} = \sum_{n=1}^{5} \frac{\beta_i^p \beta_i^q}{(\max_p \beta_i^p)^2} |\boldsymbol{C}_i^{pq}|, \tag{2.17}$$

where

$$\beta_i^p = \max_n(\Theta_i^p(\xi_n)), \quad \beta_i^q = \max_n(\Theta_i^q(\xi_n)). \tag{2.18a,b}$$

2.4. *Circulation analysis*

To quantify how the fluid is affected by variations in the effective flexibility, an analysis of the circulation around specific contours was performed. Following the methods of Colin *et al.* (2012) and Hoover *et al.* (2017), we computed the circulation, Γ, as the integral of the vorticity component normal to a planar region $\mathcal{R}$ bounded by a rectangular contour as

$$\Gamma = \int_{\mathcal{R}} \omega_y \, \mathrm{d}x \, \mathrm{d}z, \tag{2.19}$$

or

$$\Gamma = \int_{\mathcal{R}} \omega_z \, \mathrm{d}x \, \mathrm{d}y, \tag{2.20}$$

depending on the orientation of interest.

2.5. *Non-dimensional parameters*

In this study, the panels' swimming performance is examined using a number of non-dimensional metrics (table 2). Throughout a simulation, the average forward swimming speed V of material points of the panel is recorded. This is non-dimensionalized as

$$\bar{V}(t) = V(t)/c\phi, \tag{2.21}$$

which corresponds to body lengths per heaving cycle. The total force integrated over the panel, $\mathcal{F} = (\mathcal{F}_x, \mathcal{F}_y, \mathcal{F}_z)$, is also recorded and we define the non-dimensional thrust as

$$\bar{T}(t) = \mathcal{F}_x(t)/(\rho\phi^2 c^4). \tag{2.22}$$

Here we choose ϕc as a characteristic velocity, due to the absence of a background flow. Non-dimensional input power is also calculated,

$$\bar{P} = \mathcal{F}_z V_{LE}/\rho a^4 \phi, \tag{2.23}$$

using the heaving amplitude as the characteristic length and V_{LE} as the leading edge velocity. The Eulerian variables have non-dimensional analogues for flow

Effective flexibility	Π	$\sqrt{\rho s c^5 \phi^2 / EI}$
Panel velocity	$\bar{V}$	$V/c\phi$
Input power	$\bar{P}$	$P/\rho a^4 \phi$
Thrust	$\bar{T}$	$\mathcal{F}_x/\rho\phi^2 c^4$
Vorticity	$\bar{\boldsymbol{\omega}}$	$\boldsymbol{\omega}/\phi$
Flow velocity	$\bar{\boldsymbol{u}}$	$\boldsymbol{u}/c\phi$
Pressure	$\bar{p}$	$p/\rho c^2\phi^2$
Time	$\bar{t}$	$t\phi$
Swimming economy	ε	$\bar{V}_{avg}/\bar{P}_{avg}$
Inverse Strouhal number	St^{-1}	$V_{avg}/a\phi$
Input Reynolds number	Re_{in}	$\rho\phi ac/\mu$
Circulation	$\bar{\Gamma}$	$\Gamma/c^2\phi$

TABLE 2. Table of non-dimensional parameters.

velocity ($\bar{\boldsymbol{u}} = \boldsymbol{u}/c\phi$), vorticity ($\bar{\boldsymbol{\omega}} = \boldsymbol{\omega}/\phi$) and pressure ($\bar{p} = p/\rho c^2\phi^2$). Time is non-dimensionalized with respect to the heaving frequency ($\bar{t} = t\phi$). The circulation, Γ, is non-dimensionalized with respect to the chord length, c, and heaving frequency, ϕ,

$$\bar{\Gamma} = \frac{\Gamma}{c^2\phi}. \tag{2.24}$$

See table 2.

Other metrics are used to quantify a panel's performance. The swimming economy, which is the energy cost per unit of distance travelled, is defined here as

$$\varepsilon = \bar{V}_{avg}/\bar{P}_{avg}, \tag{2.25}$$

where $\bar{V}_{avg}$ and $\bar{P}_{avg}$ are, respectively, the non-dimensional speed and input power averaged over the duration of a panel's heaving cycle. We also consider the Strouhal number,

$$St = \frac{a\phi}{V_{avg}} \tag{2.26}$$

as another performance metric. Swimming and flying animals have been characterized as achieving peak propulsive efficiencies for $0.2 < St < 0.4$ (Taylor, Nudds & Thomas 2003).

The Reynolds number is a non-dimensional parameter that characterizes the ratio of inertial force to viscous forces. In this study, we report the Reynolds number using a frequency-based definition,

$$Re_{in} = \frac{\rho a\phi c}{\mu}, \tag{2.27}$$

where $a\phi$ is the characteristic velocity. Note that we use a frequency-based characteristic velocity rather than the resulting swimming speed so that Re_{in} is an input value known at the start of a simulation. In this simulations presented in this study, the maximum value of Re_{in} is 750. Alternatively, using the resulting average swimming speed of an untethered panel as a characteristic velocity would yield Reynolds numbers that are at most 1500.

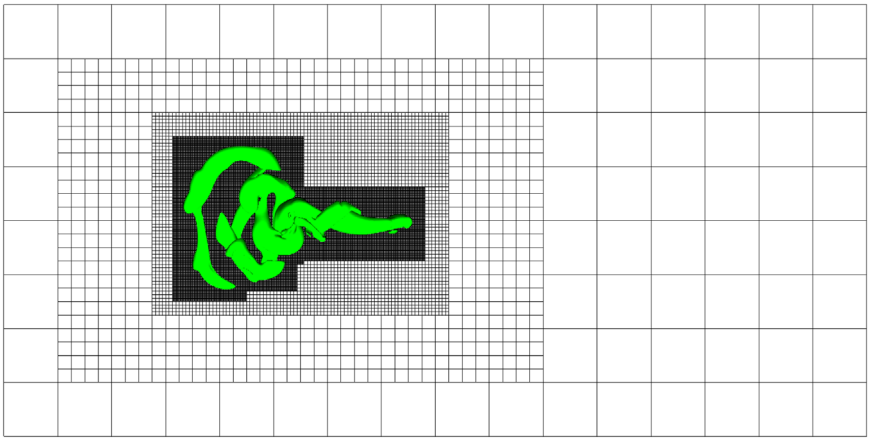

FIGURE 1. (Colour online) Plot displaying the domain discretization using adaptive mesh refinement from IBAMR, where the most refined discretization is reserved for portions of the domain where the structure is present and the vorticity magnitude is above a certain threshold, here plotted for $|\bar{\omega}| > 4$.

2.6. *Computational implementation*

The numerical model was implemented using IBAMR, which is a distributed-memory parallel implementation of the IB method that includes Cartesian grid adaptive mesh refinement (AMR) (IBAMR 2014). IBAMR relies on several open-source libraries, including SAMRAI (Hornung, Wissink & Kohn 2006; SAMRAI 2007), PETSc (Balay *et al.* 1997, 2009), *hypre* (Falgout & Yang 2002; HYPRE 2011) and `libMesh` (Kirk *et al.* 2006).

The computational domain was taken to be a rectangular box of length $8c \times 4c \times 4c$ with periodic boundary conditions in the axial direction and no-slip boundary conditions otherwise. The domain was discretized using an adaptively refined grid for which the finest Cartesian grid domain discretization would result in a $1024 \times 512 \times 512$ patch (figure 1), where the finest spatial grid size is $h = 4c/512$. The time step was taken to be $\Delta t = 1 \times 10^{-4}$ s and 5×10^{-5} s, where the latter, more refined step size was used for panels with bending moduli of 1×10^{-6} and 5×10^{-7} N m^2. Comparing the simulations with domain discretizations of $512 \times 256 \times 256$, $2048 \times 1024 \times 1024$ and $4096 \times 2048 \times 2048$ patches, we found better than linear convergence of the resulting panel swimming speed ($O(h^{1.3})$). Further convergence studies of the IBAMR method and framework can be found in Griffith & Luo (2016) and Tytell *et al.* (2016). We note that for all simulations the computational domain has been chosen large enough so that there is no discernible interaction between the panel and the boundaries of the computational domain.

3. Results

In this study, model panels with varying rigidity (see table 1) were heaved sinusoidally at an amplitude of $a = 0.1c$, with heaving frequencies that ranged from 0.125 to 3.0 s^{-1} in 0.125 s^{-1} increments. The panel begins at rest in a domain of quiescent flow and is then heaved with the body force described in (2.10) and (2.11).

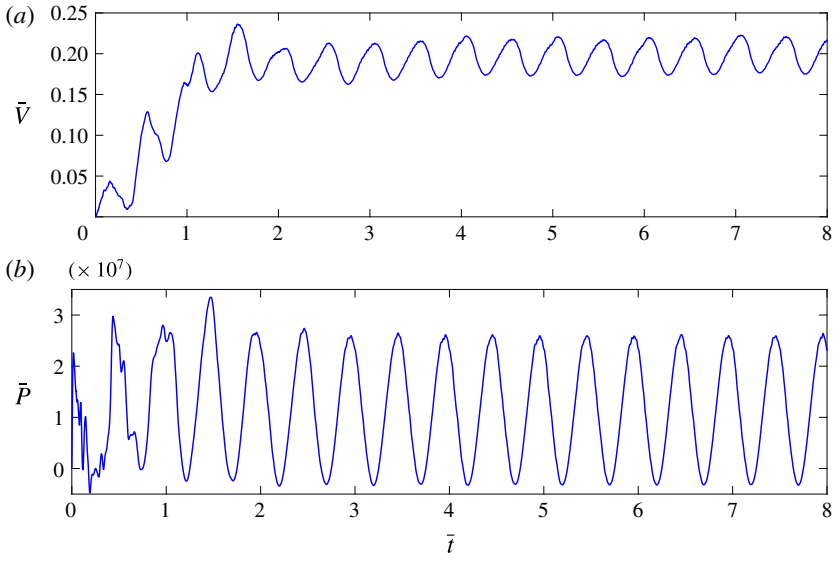

FIGURE 2. (Colour online) Plots of (*a*) dimensionless swimming speed ($\bar{V}$) and (*b*) input power ($\bar{P}$) for an untethered panel with a bending modulus of $EI = 1 \times 10^{-7}$ N m^2 being heaved sinusoidally with a frequency of $\phi = 0.5$ s^{-1}. Here $Re_{in} = 125$. Note that the panel stabilizes after the third cycle.

Figure 2 shows the time evolution of non-dimensional panel speed ($\bar{V}$) and input power ($\bar{P}$) as a function of heaving cycles for a representative panel ($EI = 1 \times 10^{-7}$ N m^2, $\phi = 0.5$ s^{-1}). After approximately two heaving cycles the velocity of the panel reaches a steady periodic state. Input power also reaches a steady-state cycle (figure 2*b*).

We also compared the cycle-to-cycle swimming performance of panels with different bending moduli or actuated at different frequencies (figure 3). In all of the simulations, the panel quickly reaches a steady-state behaviour following the initial heaving cycles, where cycle-to-cycle variations of the swimming speed are minimal. In figure 3(*a*) the swimming speed is plotted as a function of cycle number for the same panel actuated at different frequencies. Note that the swimming speed of this panel does not increase monotonically as frequency increases. This is because the resulting waveform of the panel is different for different heaving frequencies. This will be more closely examined below. In figure 3(*b*), swimming speed is plotted for three different panels of varying bending moduli that were actuated at the same frequency. There is not a monotonic change in swimming speed with respect to bending modulus. Clearly there is an interplay between the elastic properties of the panel and the fluid forces that it experiences at different frequencies. In the following sections, we analyse the swimming performance as a function of the effective flexibility Π of the heaving panel, which is the non-dimensional parameter that characterizes this interplay.

3.1. *Propulsive performance*

We performed computational experiments on five panels that differed in bending moduli and were actuated at a range of frequencies. In each of these simulations, the

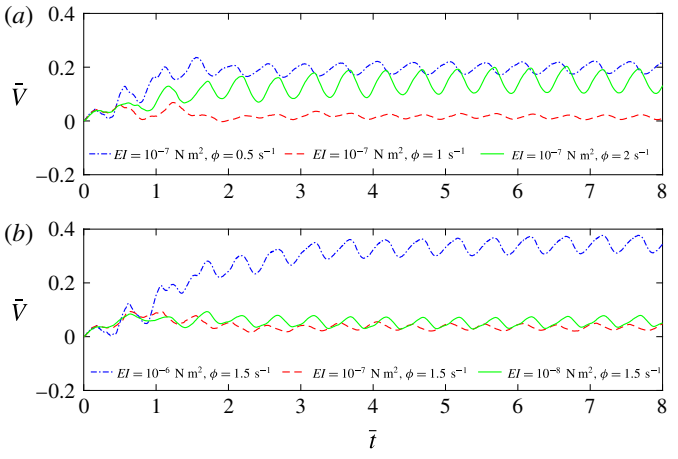

FIGURE 3. (Colour online) Comparison plots of the dimensionless swimming speed ($\bar{V}$) as a function of the cycle for three panels where (a) the bending modulus (EI) is fixed and the heaving frequency (ϕ) is varied, and (b) the heaving frequency is fixed and the bending modulus is varied.

shape of the untethered panel and its swimming progression emerge from the full coupled system. For each of the five panels, figure 4(a) shows the normalized trailing edge amplitude achieved by the panel as a function of the effective flexibility as it is actuated at different frequencies. We see that peaks in trailing edge amplitude occur near certain effective flexibilities, and these basically coincide for each of the panels. Moreover, the trailing edge amplitude varied little for panels actuated with similar effective flexibilities even when their bending moduli differed. Following the classic definition (Den Hartog 1985) and more recently that by Quinn *et al.* (2014*b*), we refer to the system as operating in resonance when the trailing edge amplitude reaches a local maximum at certain values of the effective flexibility Π (or, equivalently, the oscillation frequency ϕ). Figure 4(a) shows that there are at least four such resonant peaks in the range of effective flexibilities that we studied.

The peaks in trailing edge amplitude correspond to peaks in average swimming speed. Figure 4(b) shows the average (dimensional) swimming speed V_{avg} as a function of effective flexibility. Although the peaks in V_{avg} and trailing edge amplitude occur at similar effective flexibilities, the resulting swimming speeds depend on the bending moduli of the panel. Stiffer panels had higher V_{avg} compared to the more flexible panels heaved at similar effective flexibilities. Of course, different material panels must be actuated at different frequencies in order to achieve the same effective flexibility. Figure 4(c) shows the swimming speed divided by $c\phi$, which corresponds to body lengths per heaving cycle ($\bar{V}_{avg}$). We see that this non-dimensional velocity is better matched for panels actuated at similar effective flexibilities, but the most flexible panels still move more slowly.

In figure 5(a), we plot the average input power $\bar{P}_{avg}$, and we note that local peaks of input power coincide with local peaks in velocity (figure 4b) – the highest swimming speeds require the most power input. Figure 5(b) plots the swimming economy as a function of effective flexibility. While the peaks of average velocity and power occur at the same value of effective flexibility, the swimming economy, which is the ratio of these values, need not achieve a local maximum there. In fact, we find that the peak

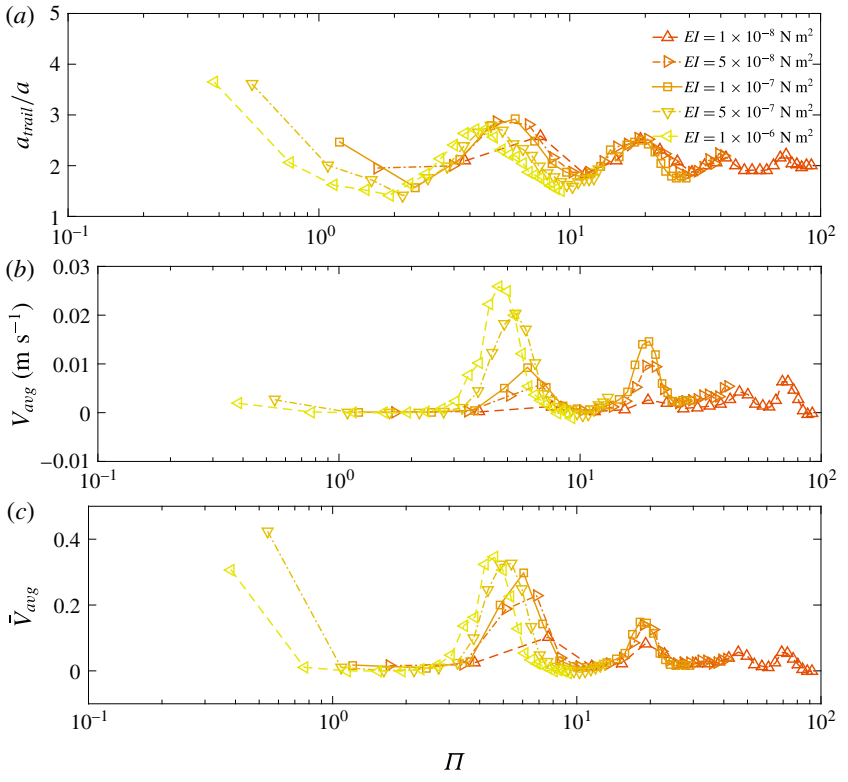

FIGURE 4. (Colour online) Plots of (*a*) trailing edge amplitude, (*b*) forward swimming speed (V_{avg}) and (*c*) dimensionless forward swimming speed ($\bar{V}_{avg}$) as a function of the effective flexibility (Π) of a panel. Here the different coloured lines represent the differing bending moduli (EI) of the panels. The range of effective flexibility values were spanned by varying the heaving frequency (ϕ) of a panel from 0.125 s^{-1} to 3.0 s^{-1}.

in economy occurs at slightly higher values of Π because the amplitude tapers off more slowly than power as Π increases. Similar shifts in efficiency peaks were noted in the model of Michelin & Llewellyn Smith (2009). We also see that input power is higher for stiffer panels than more flexible panels near the same effective flexibility. This in turn leads stiffer panels to have peaks in swimming economy at lower effective flexibilities than more flexible panels and to have a lower swimming economy overall compared to more flexible panels, even at the same effective flexibility. Note that to achieve a fixed effective flexibility, a stiff panel must be heaved at a higher frequency than a more flexible panel. This would increase the power required to complete the heaving motion. However, stiffer panels have a higher inverse Strouhal number than more flexible ones figure 5(*c*). While each tailbeat results in greater forward motion when compared to the tailbeat of a more flexible panel, more energy is expended for the motion. We plot inverse Strouhal numbers rather than Strouhal numbers, because at very low swimming speeds, the Strouhal number approaches infinity. The stiffest panels actuated so that their effective flexibilities are near the first two resonant peaks reach Strouhal numbers in the range associated with peak propulsive efficiency, $0.2 < St < 0.4$ (Taylor *et al.* 2003).

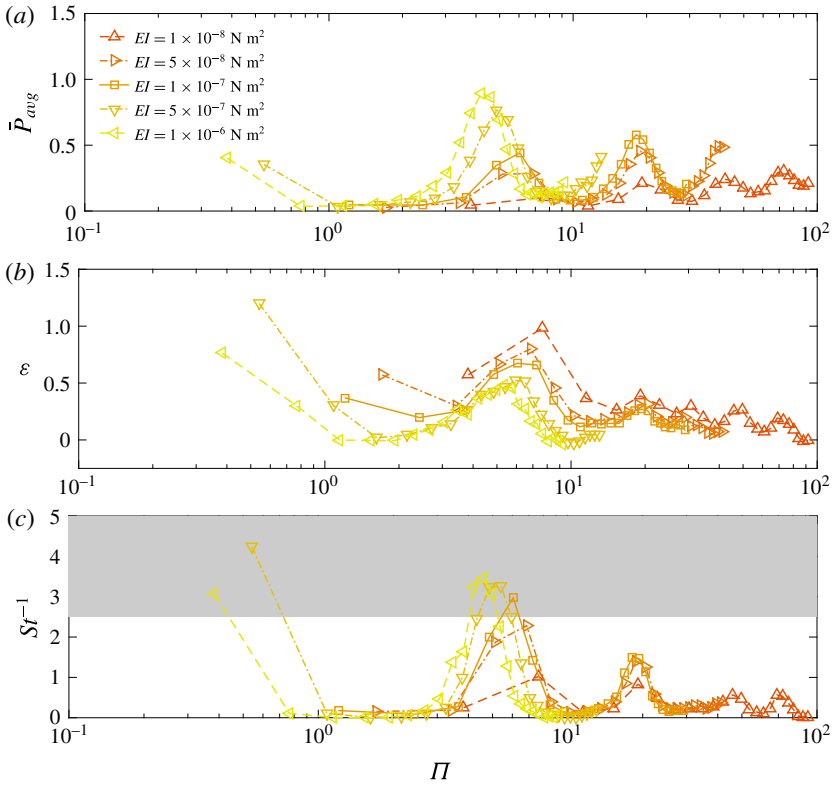

FIGURE 5. (Colour online) Plots of the panels' (*a*) average power consumption ($\bar{P}_{avg}$), (*b*) swimming economy (ε), and (*c*) inverse Strouhal number (St^{-1}) as a function of the effective flexibility (Π) of the panels. We find that for fixed Π value, the more flexible panel has a higher swimming economy. The inverse Strouhal number reveals that the two stiffest panels actuated at effective flexibilities near the first two resonant peaks correspond to the range of Strouhal numbers (in grey) associated with high efficiency swimming and flying (Taylor *et al.* 2003).

3.2. *Modal contributions*

By choosing a cross-section down the middle of the panel and averaging over its thickness, we can represent its emergent, time-periodic oscillations by a one-dimensional curve. This curve can be decomposed into the eigenfunctions of the beam equation as discussed in § 2.3. For each simulation, the first five modal contributions of the heaving panel ($\Theta_i(t)$, $i = 1, 2, 3, 4, 5$) were calculated at every time step. Figure 6(*a*) shows the time-dependent modal contributions of a representative panel simulation ($EI = 1 \times 10^{-7}$ N m^2, $\phi = 0.5$ s^{-1}) as it moves through eight heaving cycles. Each Θ_i represents the weight of the eigenfunction, Ψ_i, with respect to the deflection of the panel. Following the initial heaving cycles, all of the panel's modal contributions tend toward steady cycles. Although each of the modal contributions have the same frequency as the heaving frequency, they differ in both amplitude and phase.

The amplitude and phase of each mode depends on the effective flexibility. Figure 6(*b*) shows the shape of the panel when approximated only by the contribution of the first mode, Θ_1 (in red), over the phase $\xi \in [0, 1)$, for three panels of

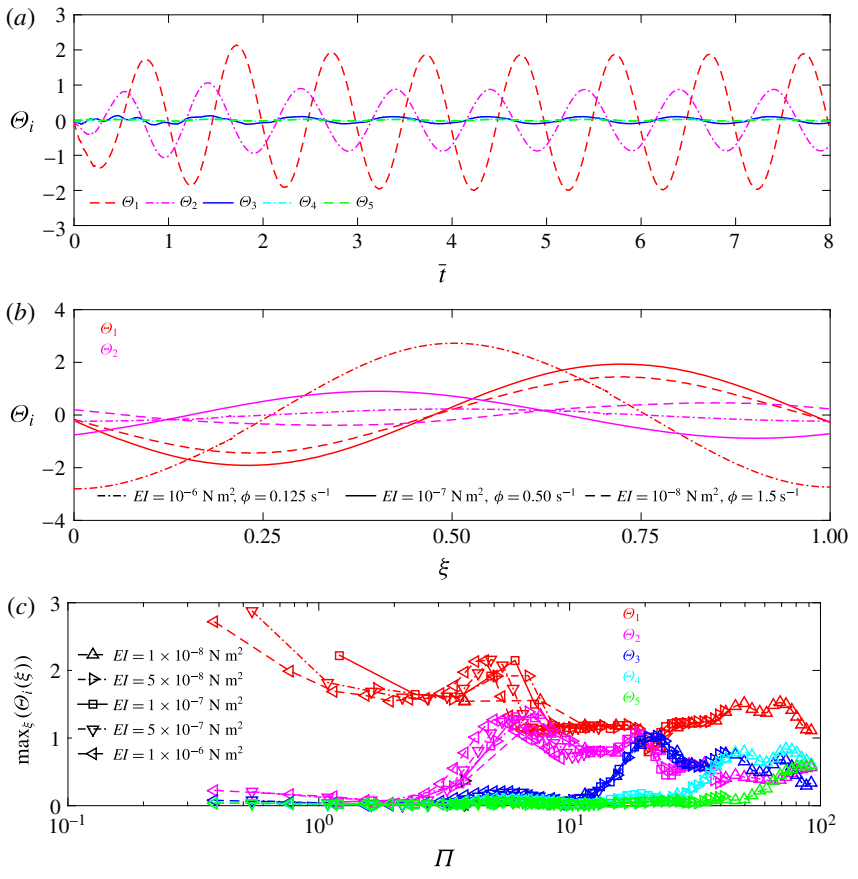

FIGURE 6. (Colour online) (*a*) Plot of the modal contribution of the first five modes with respect to the heaving cycles of a panel ($EI = 1 \times 10^{-7}$ N m^2, $\phi = 0.5$ s^{-1}). Starting from rest initially, the modal contributions of the panel deflection quickly follow a sinusoidal pattern, with each modal contribution varying in amplitude and peak point in the phase. (*b*) Plots of the modal contributions of the first (red) and second (magenta) mode for three different panels. (*c*) Plot of the maximum modal contribution of each mode with respect to the heaving panels' effective flexibility. Higher mode contributions increase as effective flexibility increases.

differing effective flexibilities ($EI = 1 \times 10^{-6}$ N m^2, $\phi = 0.125$ s^{-1}; $\Pi = 0.3827$, $EI = 1 \times 10^{-7}$ N m^2, $\phi = 0.5$ s^{-1}; $\Pi = 4.8412$ and $EI = 1 \times 10^{-8}$ N m^2, $\phi = 1.5$ s^{-1}; $\Pi = 45.9279$). For the two most flexible panels, Θ_1 has a similar amplitude and phase, while that for the third one is shifted and has a larger amplitude. Figure 6(*b*) also shows the contribution of the second mode to the panel's shape, Θ_2 (in magenta). We see that the similarities between the more flexible panels are absent in the second mode, with significant differences in amplitude and phase in Θ_2 for all three panels.

As the effective flexibility increases, each of the higher-order modes emerge sequentially, and each new mode contributes to a resonant peak in amplitude and performance. Figure 6(*c*) shows the maximum contribution of each mode, $\max_\xi(\Theta_i(\xi))$, for all panels. At lower effective flexibilities, the modal contribution from the first mode dominates, indicating that the higher modes contribute little to the shape of the panel. As effective flexibility increases, the modal contributions of

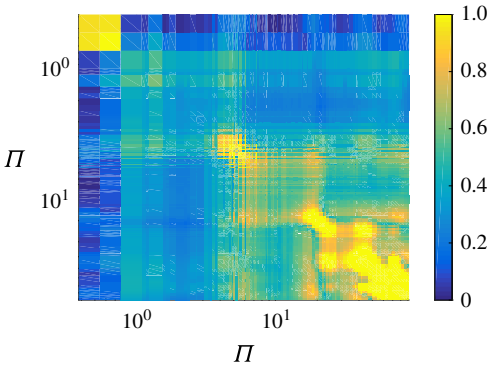

FIGURE 7. (Colour online) Q value from (2.17) associated with two panels, ordered by the two panels' effective flexibility. Note that higher Q values indicated that the modes of two panels are correlated and that the amplitude of modal contributions associated with both panels are substantial.

higher modes emerge sequentially. Their emergence is followed by a peak in the maximum modal contribution of that mode. The effective flexibilities at which a peak modal contribution occurs coincide with the effective flexibilities where peak trailing edge amplitudes and velocities occur (compare to figure 4).

3.3. *Phase evolution*

Not only are the amplitudes of the modal contributions similar when the effective flexibility is the same, but the evolution of the mode over the cycle is also similar. In figure 6(*b*), the maximum modal contributions of the first mode of two panels ($EI = 1 \times 10^{-7}$ N m^2, $\phi = 0.5$ s^{-1} and $EI = 1 \times 10^{-8}$ N m^2, $\phi = 1.5$ s^{-1}) occurred at similar phase, while the maximum modal contributions for the third panel ($EI = 1 \times 10^{-6}$ N m^2, $\phi = 0.125$ s^{-1}) occurs at a different phase. To quantify the similarity or difference in the evolution of the mode shapes for different panels, we used (2.17) to compute a normalized correlation Q^{pq} between panels p and q. This value is high when the phase evolution of the ith mode is correlated in the phase between the two panels and has a large amplitude.

Figure 7 shows the value of Q for all pairs of heaving panels arranged by effective flexibility. The high Q values along the diagonal show that panels with good swimming performance and high amplitude modal contributions have a similar shape evolution over the phase as panels with similar effective flexibilities. These correspond to the peaks in trailing edge amplitude (figure 4*a*) and swimming speed (figure 4*c*). This suggests that panels with high $\bar{V}_{avg}$ and similar Π also have similar shape evolutions over the phase of the heaving cycle. The exact locations of the resonant peaks vary slightly as a function of the panel's bending rigidity, accounting for relatively high Q values off the diagonal at $\Pi \approx 8$.

3.4. *Flow patterns*

The fluid flow resulting from the panels' heaving motion is examined via dimensionless vorticity, $\bar{\omega}$. Figure 8 shows an example of the development of the flow in the first four heaving cycles. Although the vortex structures present in the wake grow after each heaving cycle, the shape of the panel at the start of the cycle and the vortex

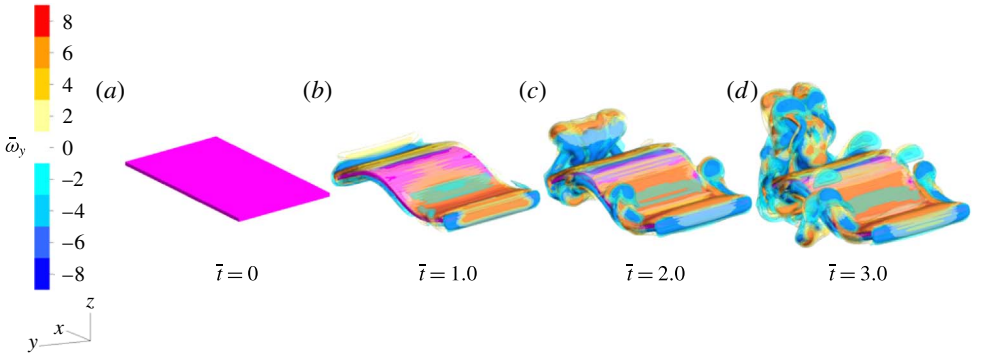

FIGURE 8. (Colour online) Isocontour plots of the dimensionless y-component of vorticity, $\bar{\omega}_y$, at the start of the first through fourth heaving cycles (from left to right). The panel is of $\Pi = 19.3649$ ($EI = 1 \times 10^{-7}$ N m^2, $\phi = 2.0$ s^{-1}) and $Re_{in} = 500$. Note that after the first heaving cycle, the deflection of the panel is nearly identical at the start of each heaving cycle, although the resulting vorticity field varies in time.

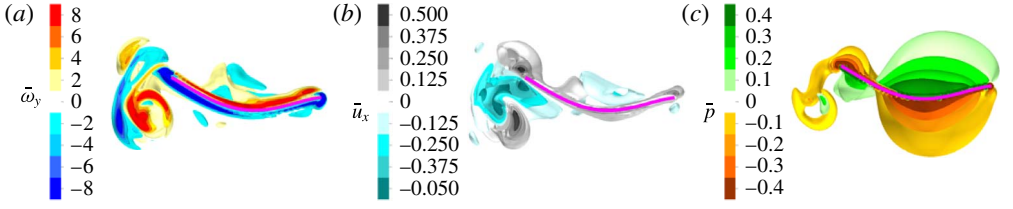

FIGURE 9. (Colour online) Isocontour plots, cut out along the centre plane, of the (*a*) dimensionless y-component of vorticity ($\bar{\omega}_y$), (*b*) dimensionless x-component of flow velocity ($\bar{u}_x$) and (*c*) dimensionless pressure ($\bar{p}$) during the start of the third heaving cycle of a panel with $\Pi = 6.0515$ ($EI = 1 \times 10^{-7}$ N m^2, $\phi = 0.625$ s^{-1}).

structures in the immediate wake remain fairly constant following the initial heaving cycle.

In figure 9, we compare the isocontours along the centre plane for the spanwise (y) vorticity ($\bar{\omega}_y$), axial (x) velocity ($\bar{u}_x$) and pressure ($\bar{p}$) at the start of the third heaving cycle for a panel with a substantial swimming speed ($EI = 1 \times 10^{-7}$ N m^2, $\phi = 0.625$ s^{-1}). The trailing edge generates alternating vortex structures (figure 9*a*). These vortices then generate a region of positive axial flow ($\bar{u}_x$) near the trailing edge of the panel (grey region in figure 9*b*). This zone of positive axial velocity corresponds to the presence of positive pressure near the trailing edge of the panel and negative pressure on the opposite side (figure 9*c*), which combine to give the thrust force. We also find zones of positive and negative pressure on opposite sides of the panel due to the deflections of the panel.

Differences in the panel shape evolution yield differences in the resulting flow structures. Figure 10 compares the $\bar{\omega}_y$ isocontours at the start of the third heaving cycle for three panels, with differing passive material properties and identical heaving frequencies. The differences in the observed flow structures in turn account for differences in panel performance. Similar observations can be made when examining $\bar{\omega}_y$ isocontours of three panels with identical passive material properties but differing

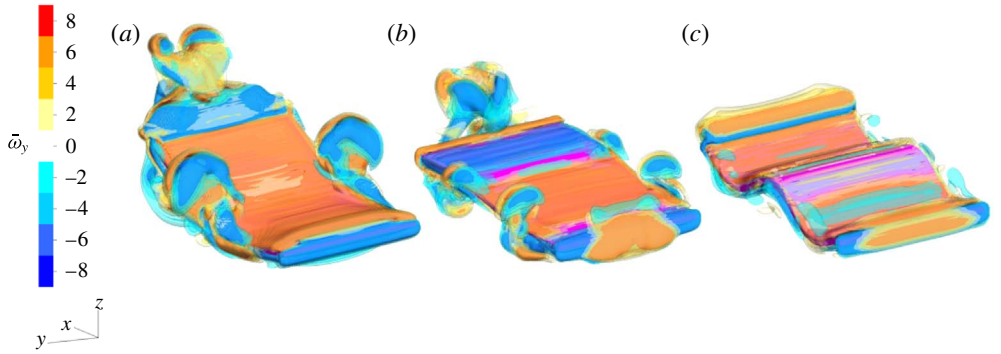

FIGURE 10. (Colour online) Isocontour plots of the dimensionless y-component of vorticity, $\bar{\omega}_y$, at the start of the third heaving cycle for three panels heaved at the same frequency, $\phi = 1.5$ s^{-1}, but with EI equal to (a) 1×10^{-6} N m^2 ($\Pi = 4.5928$), (b) 1×10^{-7} N m^2 ($\Pi = 14.5237$), (c) 1×10^{-8} N m^2 ($\Pi = 45.9279$).

heaving frequencies. Movies of both comparisons can be found in the supplementary material available at https://doi.org/10.1017/jfm.2018.305.

Above we have shown that panels with similar effective flexibility Π have similar performance. This is because they produce similar flow patterns. Figure 11 shows phase-matched snapshots of the isocontours of $\bar{\omega}_y$ for three panels with similar effective flexibilities ($\Pi \approx 6$). Although of similar effective flexibility, the three panels all differ with respect to their heaving frequency and bending modulus. Because the deflections of the panels are similar throughout the phase of the heaving cycle, the dominant vortex structures found in the wake of each of the three panels are also similar. Minor variations in vortex structures of the wakes of the three panels correspond to differences in Re_{in}, with the presence of more vortex structures in the higher Re_{in} case (figure 11a). Movies of these comparisons, as well as a comparison of other panels of similar effective flexibilities and high dimensionless swimming speeds, can be found in the supplementary material.

The structure of the wake changes for panels at values of Π that correspond to peaks in swimming speed. Figure 12 plots the $\bar{\omega}_y$ isocontours and figure 13 shows slices through the central plane, each for three swimmers with Π values associated with three different peaks in $\bar{V}_{avg}$. The three panels each have high dimensionless forward swimming speeds but substantially differing deflections. The more flexible panels (figure 13b,c) shed two pairs of vortices per cycle (a 2P wake structure; Williamson & Roshko 1988), while the stiffer panel (figure 13a) sheds two single vortices per cycle (a 2S wake).

To further explore how fluid effects allow for differences in swimming performance even when panels are of a similar Π value, we examined the differences in circulation for the panels of figure 11 ($\Pi \approx 6$). We found that the panels reached peak swimming speeds near phase $\xi = 0.25$ during the heaving cycle. We also examined $|\bar{\boldsymbol{\omega}}|$ (figure 14) and found the presence of a vortex column at the trailing edge of the panel as well as tip vortices near the halfway point of the panels' chordwise dimension.

The presence and sign of $\bar{\omega}_z$ in the tip vortices (figure 15) indicate a source of additional drag on the panel as the flow generated by $\bar{\omega}_z$ is against the swimming direction of the panel. We computed the circulation (figure 16a) around a contour enclosing the trailing edge vortex and lying on the centre plane $y = 0$ as well as the

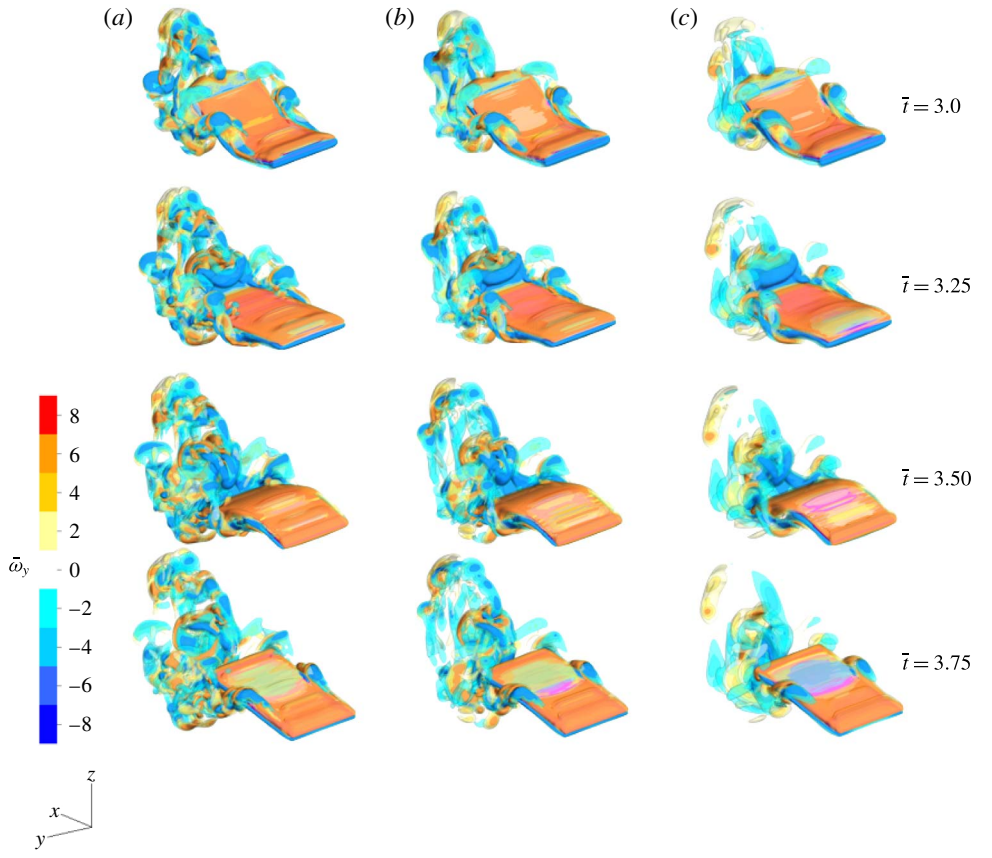

FIGURE 11. (Colour online) Isocontour plots of the dimensionless y-component of vorticity, $\bar{\omega}_y$, during the heaving cycle for three panels of similar effective flexibility, with Π equal to (*a*) 5.7410 ($EI = 1 \times 10^{-6}$ N m^2, $\phi = 1.625$ s^{-1}, $Re_{in} = 406.25$), (*b*) 5.4127 ($EI = 5 \times 10^{-7}$ N m^2, $\phi = 1.250$ s^{-1}, $Re_{in} = 312.5$), (*c*) 6.0515 ($EI = 1 \times 10^{-7}$ N m^2, $\phi = 0.625$ s^{-1}, $Re_{in} = 156.25$). Snapshots are taken at $\bar{t}$ (from top to down) 3.0, 3.25, 3.50 and 3.75.

circulation of the tip vortices around a contour lying on the xy-plane enclosing the tip vortices. Plotting $\bar{\Gamma}$ of the trailing edge vortex as a function of Re at $\xi = 0.25$ (figure 16*b*), we found that this circulation was approximately equal for the three panels. However, the circulation of the tip vortices was larger for panels with larger Re (figure 16*b*). This suggests that the tip vortices play a role in the observed differences in the swimming economy, where stiffer panels that move faster (higher Re) are less efficient than slower, more flexible panels of a similar Π.

3.5. *Spanwise variation*

In order to gain insight into the effects of tip vortices on swimming performance, we chose a reference panel and varied its span length. From (2.9) and (2.14), we note that Π is not dependent on the span of the panel,

$$\Pi = \sqrt{\frac{12\rho c^4 \phi^2 (1 - \nu^2)}{E w^3}}. \tag{3.1}$$

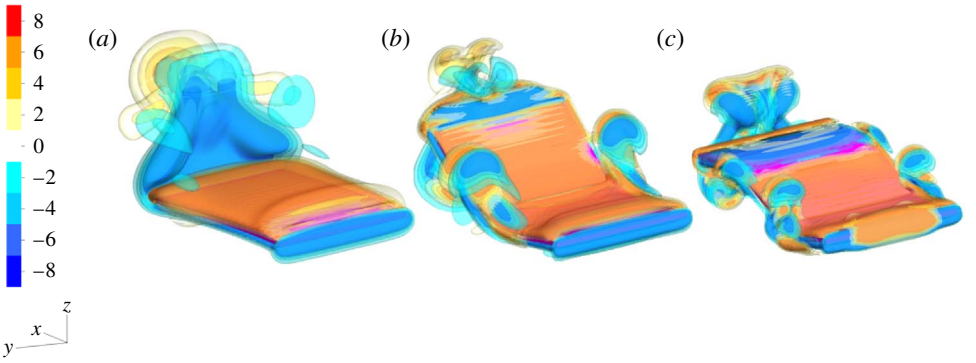

FIGURE 12. (Colour online) Isocontour plots of the dimensionless y-component of vorticity, $\bar{\omega}_y$, at the start of the third heaving cycle for three panels that swim rapidly but have different effective flexibilities, Π equal to (a) 0.5413 ($EI = 5 \times 10^{-7}$ N m^2, $\phi = 0.125$ s^{-1}, $Re_{in} = 31.25$), (b) 6.0515 ($EI = 1 \times 10^{-7}$ N m^2, $\phi = 0.625$ s^{-1}, $Re_{in} = 156.25$), (c) 17.116 ($EI = 5 \times 10^{-8}$ N m^2, $\phi = 1.250$ s^{-1}, $Re_{in} = 312.5$).

A high performing panel with a Π value associated with the second mode resonance was chosen as the reference case ($EI = 1 \times 10^{-7}$ N m^2, $\phi = 0.625$ s^{-1}). We compare the performance of the reference panel with aspect ratio $s/c = 0.6$, and two others of aspect ratios 0.2 and 1.0, each with the same effective flexibility. Additionally, a simulation of a heaving filament in a two-dimensional fluid domain was performed, corresponding to the case free of tip vortices and infinite aspect ratio.

As the span of the panel increases, the swimming performance increases. In figure 17(a) the swimming speed was found be highest for the two-dimensional panel, with swimming speed for the three-dimensional cases approaching this level as the span length increased. Measuring the circulation of the tips for the three-dimensional cases (figure 17b), we found the circulation measured increases slightly as the span decreases, where the panel with an aspect ratio of 0.2 has an 8 % increase circulation relative to the reference panel. This suggests that the additional drag generated from the tip vortices plays a relatively larger role as the span decreases.

3.6. *Comparison between tethered and free-swimming panels*

Do the peaks in the swimming speeds of an actuated, untethered panel correspond to the peaks in the thrust generated by the same actuated panel that is tethered and not free to swim? To examine this, we performed a set of simulations of tethered panels at the same heaving frequencies and five bending moduli as in untethered simulations. In this set of simulations, a tethered body force was applied to the leading edge and the panel was heaved until its motion reached a steady state. Figure 18(a) shows the maximum modal contributions of the first five modes computed from the emergent geometries of the tethered panels. We find that the peaks in these modal contributions correspond to the peaks observed for the freely swimming panels shown in figure 6(c). In addition, for these tethered panels the resulting forces $\mathcal{F}$ from the heaving motion were recorded and used to compute the resulting non-dimensional forward thrust $\bar{T}$. This thrust was then averaged over a heaving cycle ($\bar{T}_{avg}$). Figure 18(b) shows the thrust developed by each of the five tethered panels as a function of the effective flexibility. We find that peaks in $\bar{T}_{avg}$ occur near the same values of effective flexibility that displayed peaks in forward swimming speed for the corresponding untethered

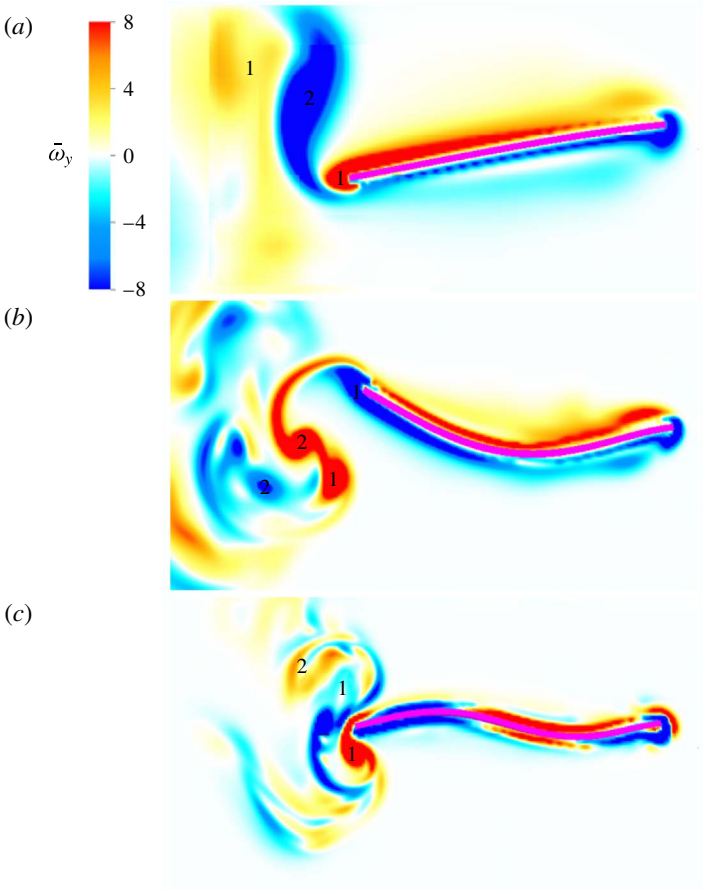

FIGURE 13. (Colour online) Plots of the dimensionless y-component of vorticity along the central plane at the end of the fourth heaving cycle for panels with Π equal to (*a*) 0.5143 ($EI = 5 \times 10^{-7}$ N m^2, $\phi = 0.125$ s^{-1}), (*b*) 6.0515 ($EI = 1 \times 10^{-7}$ N m^2, $\phi = 0.625$ s^{-1}) and (*c*) 17.116 ($EI = 5 \times 10^{-8}$ N m^2, $\phi = 1.25$ s^{-1}). The three panels are representative of the panels with Π values associated with the first three resonant peaks. In (*a*) we note the presence of a 2S vortex shedding pattern, while in (*b*,*c*) the 2P vortex shedding pattern is present.

simulations (see figure 4*c*). These peaks in turn correspond to local peaks in the modal contributions.

We also use the tethered panel framework to validate our simulation results by comparing predictions of peaks in thrust with analytical approximations from a linearized theory. Van Eysden & Sader (2006, 2007, 2009) developed a theory for the frequency response of a cantilever beam with rectangular cross-section immersed in a viscous fluid. In that study the fundamental frequencies are a function of panel geometry, EI and Reynolds number, and are based on the exact solution of the linearized Navier–Stokes equations produced by a zero-thickness, infinitely long oscillating blade. It is noted in Van Eysden & Sader (2007) that these approximations to harmonic response frequencies become less accurate as the mode increases due to the heightened three-dimensional aspects of the cantilever–fluid system. As a way of validating our method, we compare the frequencies at which the tethered panels

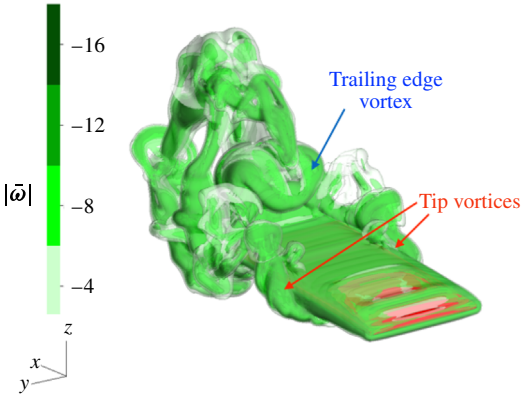

FIGURE 14. (Colour online) Plot of the dimensionless vorticity magnitude, $|\bar{\omega}|$, near the point of peak panel swimming speed for a panel with $\Pi = 5.7410$ ($EI = 1 \times 10^{-6}$ N m^2, $\phi = 1.625$ s^{-1}, $Re_{in} = 312.5$). The tip vortices and trailing edge vortex are highlighted.

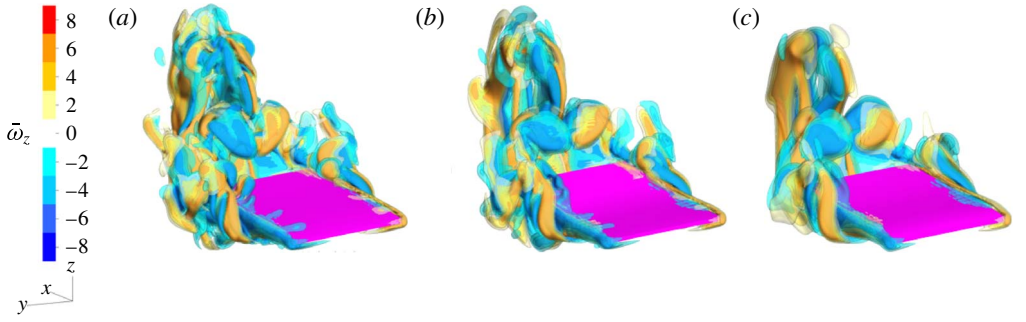

FIGURE 15. (Colour online) Isocontour plots of the dimensionless z-component of vorticity, $\bar{\omega}_z$, near the point of peak panel swimming speed during the heaving cycle for three panels with similar effective flexibilities, Π equal to (*a*) 5.7410 ($EI = 1 \times 10^{-6}$ N m^2, $\phi = 1.625$ s^{-1}, $Re_{in} = 406.25$), (*b*) 5.4127 ($EI = 5 \times 10^{-7}$ N m^2, $\phi = 1.25$ s^{-1}, $Re_{in} = 312.5$), (*c*) 6.0515 ($EI = 1 \times 10^{-7}$ N m^2, $\phi = 0.625$ s^{-1}, $Re_{in} = 156.25$).

of our simulations achieve local peaks in thrust to the values of harmonic response frequencies corresponding to different modes predicted by Van Eysden & Sader (2007). For each of our five panels with fixed geometry and different bending moduli EI, we compute the harmonic response frequencies ω_n associated with mode n using the linear theory. For that ω_n and EI, we associate an effective flexibility Π of that panel waved at the harmonic response frequency. These effective flexibilities (for five panels and the first five modes) are indicated on the horizontal axis of figure 18(*b*), and vertical lines are drawn emanating from these values. For each mode n, the theoretical values of effective flexibility are essentially equal for the different bending moduli. For the smallest values of Π that correspond to stiff panels or panels heaved at low frequencies, restrictive computational costs do not allow simulations that resolve the first mode, so we focus on modes 2–5. However, the effective flexibility corresponding to the theoretical harmonic response frequency of the second mode

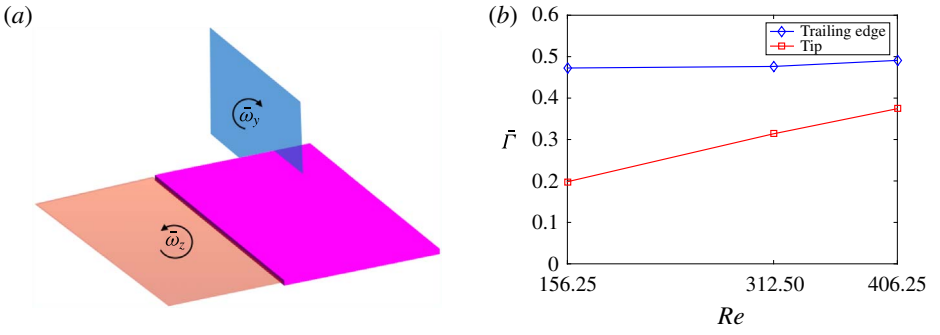

FIGURE 16. (Colour online) (*a*) Diagram of the planes from which the circulation of the trailing vortex (blue) and the tip vortices (red) were calculated. (*b*) Plot of the circulation, $\bar{\Gamma}$, of the trailing edge vortices (blue) and the tip vortices (red) for the panels of figures 11 and 15 as a function of *Re*.

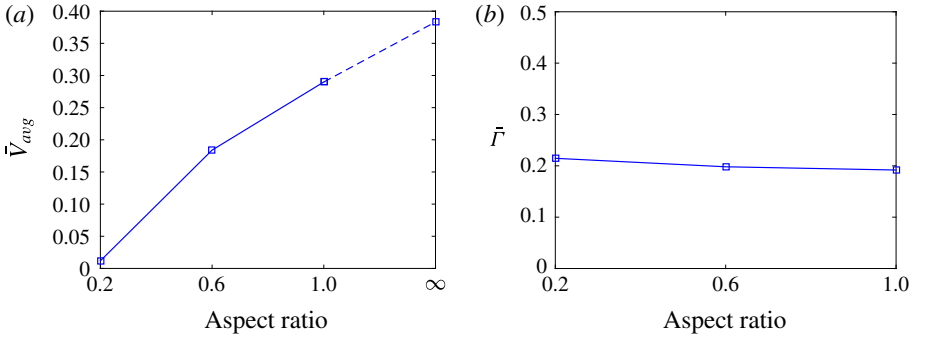

FIGURE 17. (Colour online) Plots of (*a*) the dimensionless swimming speed ($\bar{V}_{avg}$) and (*b*) the dimensionless circulation of the tip vortices ($\bar{\Gamma}$) for panels of differing aspect ratio. Here an aspect ratio of ∞ represents a two-dimensional panel. As the panel aspect ratio increases, the swimming speed increases although the strength of the tip vortices remains relatively constant.

for $EI = 1 \times 10^{-7}$ and 5×10^{-8} N m^2 differs from the simulation value of Π at which peaks occur by less than 0.3 %, and for the third mode by less than 10 %. Larger differences are associated with higher modes, as expected. For stiffer panels, $EI = 1 \times 10^{-6}$ and 5×10^{7} N m^2, the computed effective flexibilities for mode 2 are approximately 22 % lower than those predicted by the analytic model of Van Eysden & Sader (2007). The least stiff panel, $EI = 1 \times 10^{-8}$ N m^2, corresponds to a relative difference of 30 % in effective flexibilities for mode 2. The agreement between the harmonic response frequencies for modes 2 and 3 estimated by two-dimensional linear theory and those computed using the full three-dimensional Navier–Stokes system serves as a validation of the simulations.

Figure 19 show scatter plots of the thrust of a tethered heaving panel and the speed of its untethered counterpart ($\bar{T}_{avg}$, $\bar{V}_{avg}$), for the five panels. We find that for tethered panels that produce positive thrust, $\bar{T}_{avg}$, increasing thrust generally corresponds to increasing free-swimming speed $\bar{V}_{avg}$. To further examine the differences between

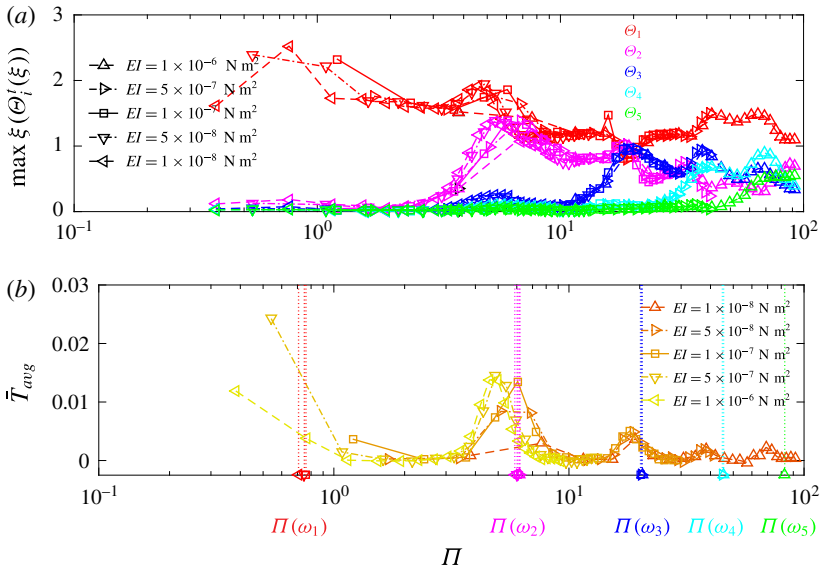

FIGURE 18. (Colour online) (*a*) Plot of the maximum modal contribution of each mode as a function of the tethered, heaving panels' effective flexibility. Higher mode contributions increase as effective flexibility increases. (*b*) Plot of the dimensionless thrust, $\bar{T}_{avg}$, as a function of the effective flexibility, Π. The effective flexibilities corresponding to the analytic prediction of the first five harmonic response frequencies (Van Eysden & Sader 2007) for the five panels are indicated by symbols on the horizontal axis, from which emanate dashed vertical lines whose colour corresponds to the five modes in panel (*a*).

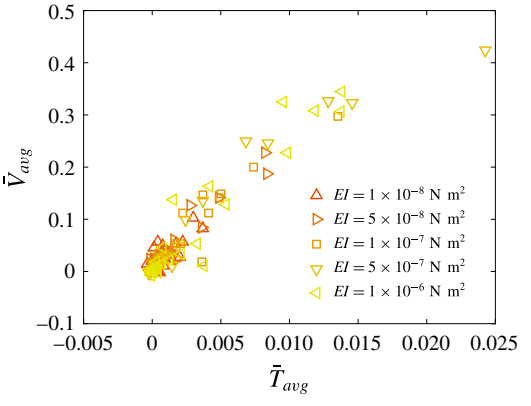

FIGURE 19. (Colour online) Plot of the maximum modal contribution of each mode with respect to the heaving panels' effective flexibility. Higher mode contributions increase as effective flexibility increases.

tethered and untethered panels, we examined the modal contributions of the tethered panels (figure 18*a*). We find that the amplitude of modal contributions of the panels have peaks at the same Π value, although the amplitude of the modal contribution varies.

4. Discussion

In this study, we developed a model of a three-dimensional, flexible panel that is heaved sinusoidally at its leading edge in a viscous fluid and used numerical simulations to study the role of resonance, fluid forces and shape evolution in the propulsive performance of the panels. As in previous experimental work on tethered panels (Quinn *et al.* 2014*b*), we found that the effective flexibility captures the main features of the elastohydrodynamic system. Even when the material properties differ substantially, panels flapping at different frequencies can have the same effective flexibility. In this case, they exhibit similar deformation patterns, both in shape and phase. This leads to similar flow patterns, which in turn result in similar non-dimensional swimming speeds.

However, there are important differences that correspond to the material properties. At the same effective flexibility, more flexible panels (lower EI) are more economical: they require less input power to swim at about the same dimensionless speed, even when the effective flexibility is approximately the same. Conversely, stiffer panels (higher EI) swim at Strouhal numbers closer to the range associated with high propulsive efficiency (Triantafyllou, Triantafyllou & Grosenbaugh 1993; Taylor *et al.* 2003). These differences may correspond to the Reynolds number Re_{in}, which is higher for stiffer panels at the same effective flexibility. This corresponds to a more complex wake, with higher forces on the panel, which leads to a greater forward speed for a given actuation, but also takes more input power and thus results in a lower economy. Similarly, our observations on how flexibility can increase the swimming economy of the panel (figure 5*b*) coincide with the observations by Dewey *et al.* (2013) that found an increase in propulsive efficiency with the addition of flexibility.

As effective flexibility Π increases, there are multiple resonant peaks in performance parameters, including tailbeat amplitude (figure 4*a*), swimming speed (figure 4*c*), thrust (figure 18*b*), along with measures of swimming energetics, including economy (figure 5*b*) and inverse Strouhal number (figure 5*c*). By decomposing the deformation into the fundamental beam bending modes, we found that each successive peak as Π increases corresponds to a peak in amplitude of a higher-order bending mode (figure 6*c*). This confirms the observations of de Sousa & Allen (2011), that higher mode contributions have a larger amplitude as the bending rigidity of the panel decreases and heaving frequency remains constant. For a fixed effective flexibility, varying the heaving frequency requires that we proportionally adjust the bending rigidity to the order $1/2$. This aligns with the findings of Michelin & Llewellyn Smith (2009), who detailed how the resonant frequency associated with each mode evolves as a function of bending rigidity.

The effective flexibility captures the presence of these resonant interactions, but the exact value differs for panels with different bending modulus. For instance, the curves in figure 4(*c*) do not collapse exactly. It is important to point out that although panels have similar effective flexibilities, the resulting dimensional swimming speed varies and can in turn adjust the location of the observed resonant peak (Quinn *et al.* 2014*b*). Another possibility for this discrepancy is that the approximation does not fully account for additional fluid drag terms when considering the solution to the Euler–Bernoulli beam equation (2.14) (Paraz *et al.* 2014; Richards & Oshkai 2015). We also note that the panels in this study are neutrally buoyant and that additional inertial terms due to mass of the panel could lower the observed performance gain due to resonance, as was observed in Yeh & Alexeev (2014).

The locations of the resonant peaks match well with those in the experimental study by Quinn *et al.* (2014*b*). Because their study and ours differ in substantial ways, this correspondence in effective flexibility supports it as a good non-dimensional parameter for the fluid–panel system. In their study, the panel was tethered and a steady-state background flow was present, with Re ranging from 7800 to 46 800, with the characteristic velocity chosen to be the steady-state background flow velocity. Our study focused on the propulsive performance of an untethered panel in quiescent flow, with the maximum Re of 1500, using the highest observed swimming speed as the characteristic velocity. Although the range of Π values was similar to that of Quinn *et al.* (2014*b*), the bending moduli of their panels were orders of magnitude higher than in our study.

We also find that for tethered panels that produce positive thrust $\bar{T}_{avg}$, increasing swimming speeds $\bar{V}_{avg}$ in untethered panels corresponds to increasing thrusts in the tethered panels. For the tethered panels in our study, there is no oncoming flow, while in most experimental studies (e.g. Quinn *et al.* (2014*b*)) there usually is a flow. This difference should not affect the overall pattern of thrust as a function of flexibility (figure 18*b*). Quinn *et al.* (2014*b*) compared thrust for panels with the same effective flexibility at different oncoming flow speeds. While the bending mode shapes changed, the amplitude and thrust did not. Recently, Van Buren *et al.* (2018) studied this effect specifically, and showed that the oncoming flow speed does not affect the way thrust changes as a function of frequency. They measured thrust production for tethered panels as they varied the oncoming flow speed over a wide range and found only small differences at different speeds, differences that were much smaller than the effect of changing foil stiffness or pitching frequency. In our simulations, we find that the positive thrust of the tethered panels corresponds linearly with the swimming speeds of the untethered panels. There were differences in the maximum modal contributions between the tethered and untethered panels, but the point in the phase where the peak modal contribution occurs is relatively unchanged. This is potentially due to the vortex structures generated during the heaving cycle that, in the tethered case, do not advect away from the panel, as would be the case with the presence of background flow, or when the panel is free to swim. This effect can be seen for the untethered panel depicted in figure 9, which shows the presence of pressure generated by the shed vortex structures near the panel's trailing edge. This pressure contributes to positive axial flow near the panel, as was observed by Green & Smits (2008). In the tethered case, the same vortex structures would have a stronger influence on the panel's deflection at the trailing edge.

We demonstrated that the effective flexibilities at which the tethered panels achieve peaks in thrust compare very well with the analytical predictions of Van Eysden & Sader (2009) for modes 2 and 3. It was noted that the harmonic response frequencies, which are derived using a linear approximation of the Navier–Stokes equations, do not necessarily correspond with the mechanical resonance exhibited by the trailing edge when a force is acting on the panels. We also note a small shift in the Π values where peak trailing edge amplitudes occur, but these values from our simulations agree closely with those of the experimental study of Quinn *et al.* (2014*b*) could affect the added mass associated with the heaving panel. The panels in our study had bending moduli EI that were generally a few orders of magnitude less than those used by Quinn *et al.* (2014*b*) and also differ in aspect ratio. A recent study by Piñeirua, Thiria & Godoy-Diana (2017) found differences in aspect ratio also yield shifts in the optimal frequencies for peak swimming speed and thrust.

The study by Alben *et al.* (2012), where two-dimensional, rectangular panels were heaved at their leading edge in an inviscid fluid, found panel swimming speed to be proportional to panel length to $-1/3$ power and bending rigidity to the $2/15$ power. Although Alben *et al.* did not directly examine the effective flexibility of their panels, they indirectly do so by adjusting the added mass and internal bending forces by varying the length and rigidity of the panel respectively. By increasing the length of the panel they increase its effective flexibility, and their observed decline in swimming speed corresponds to our observed decline in the peak swimming speeds associated with the resonant peaks at higher effective flexibilities. Similarly, increasing the bending rigidity of the panel corresponds to an decrease of the effective flexibility of the panel. Alben *et al.* (2012) also found that increasing the length of the panel or decreasing the rigidity also increased the wavenumber of the panel deflection, which corresponds to the addition of higher modal contributions as effective flexibility decreases.

Our results may help to explain some of the characteristics of biological propulsors. Lucas *et al.* (2014) found that many flexible biological propulsors tend to have the most bending approximately 0.6 of the way down their length and tended to bend at an angle of 30°. If we treat our panels as propulsors like those analysed by Lucas *et al.* (2014), with a flexion ratio of 0.6, and compute the angle formed by the trailing edge of the panel with respect to the point of inflection, $\vartheta = \tan^{-1}[(0.5a_{trail})/(0.6c)]$, we find that panels of high swimming speeds had ϑ between 26° and 40°, which are within the flexion angle ranges observed by Lucas *et al.* (2014). Qualitatively, the panels that had the most similar kinematics to those observed by Lucas *et al.* (2014) were panels near the second resonant peak (Π from 3 to 6) with substantial contributions from the first two bending modes (see figure 20*a*,*b*). We found that panels near this peak also had the highest dimensional speed (V_{avg}) compared to panels of differing effective flexibilities (figure 20*c*). These results could also explain the inverse relationship between the body size and tail beat frequency that was observed in fish swimming by Bainbridge (1958). Our results also coincide with Root & Courtland (1999), who found that pitching rubber fish models tended to have more higher-order modes at high frequencies, where fish tend to damp out the higher-order modes to improve their swimming economy.

5. Conclusion

In conclusion, the development of this three-dimensional elastohydrodynamic model of a flexible panel allows for future investigations relating to flapping propulsion, such as the propulsive benefits to non-uniform flexibility (Liu & Bose 1997; Lucas *et al.* 2014), non-sinusoidal heaving (Lehn *et al.* 2017) and variations in panel geometry (Buchholz & Smits 2006; Van Buren *et al.* 2017). The numerical investigation reaffirms the validity of tethered panel experimental studies in studying the propulsive of performance of free-swimming bodies. This reduced model of a flexible flapping panel serves as major step towards a more comprehensive computational model of an undulatory swimmer that will couple neural activation, muscle mechanics and body elasticity to fluid dynamics. Such a comprehensive model will be capable of determining how the resulting kinematics measured from observational studies of swimming and flying organisms are a consequence of the interplay of muscle contractions and passive elastic properties of a body.

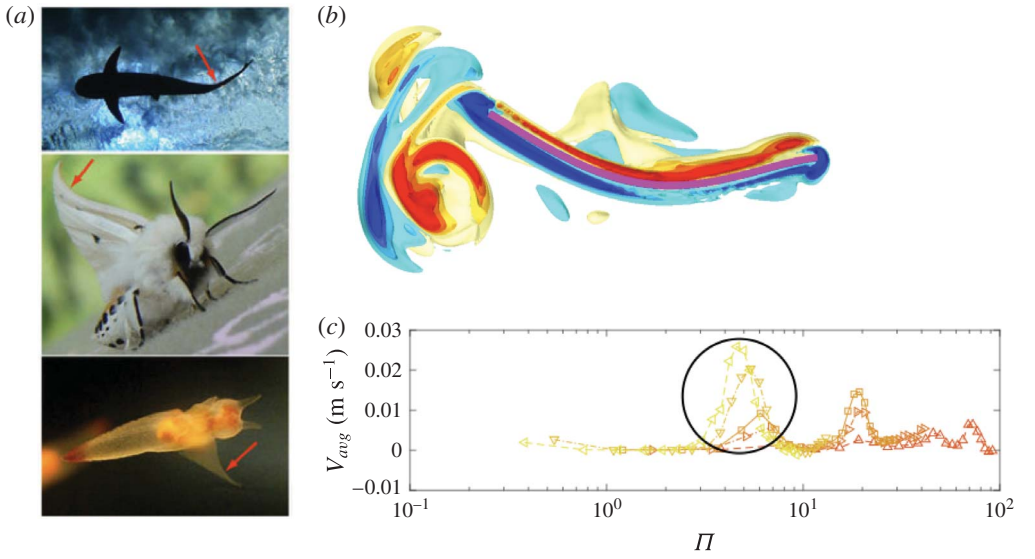

FIGURE 20. (Colour online) (*a*) Plots of the flexible propulsors of free-swimming animals, with red arrows pointing to the point of inflection, from Lucas *et al.* (2014). (*b*) The profile of a panel, with $\bar{\omega}_y$ contours, whose effective flexibility is near the resonant peak associated with first and second modal contributions, circled in (*c*).

Acknowledgements

We would like to thank M. Leftwich for comments and suggestions during the preparation of this manuscript. We would also like to thank B. Griffith for advice on implementing the model in IBAMR. This work was supported by National Science Foundation grants DMS 1043626 (to A.P.H., R.C., L.J.F.), DBI-RCN 1062052 (to Avis H. Cohen and L.J.F.) and DMS 1312987 (to E.D.T. and L.J.F.).

Supplementary movies

Supplementary movies are available at https://doi.org/10.1017/jfm.2018.305.

REFERENCES

ALBEN, S. 2008 Optimal flexibility of a flapping appendage in an inviscid fluid. *J. Fluid Mech.* **614**, 355–380.

ALBEN, S. & SHELLEY, M. 2005 Coherent locomotion as an attracting state for a free flapping body. *Proc. Natl Acad. Sci. USA* **102** (32), 11163–11166.

ALBEN, S., WITT, C., BAKER, T. V., ANDERSON, E. & LAUDER, G. V 2012 Dynamics of freely swimming flexible foils. *Phys. Fluids* **24** (5), 051901.

ANDERSEN, A., BOHR, T., SCHNIPPER, T. & WALTHER, J. H. 2017 Wake structure and thrust generation of a flapping foil in two-dimensional flow. *J. Fluid Mech.* **812**, R4.

BAINBRIDGE, R. 1958 The speed of swimming of fish as related to size and to the frequency and amplitude of the tail beat. *J. Expl Biol.* **35** (1), 109–133.

BALAY, S., ABHYANKAR, S., ADAMS, M., BROWN, J., BRUNE, P., BUSCHELMAN, K., EIJKHOUT, V., GROPP, W., KAUSHIK, D., KNEPLEY, M. & OTHERS 2009 PETSc: Web page http://www.mcs.anl.gov/petsc.

BALAY, S., GROPP, W. D., MCINNES, L. CURFMAN & SMITH, B. F. 1997 Efficient management of parallelism in object-oriented numerical software libraries. In *Modern Software Tools for Scientific Computing* (ed. E. Arge *et al.*), pp. 163–202. Springer.

BHALLA, A. P. S., BALE, R., GRIFFITH, B. E. & PATANKAR, N. A. 2013 A unified mathematical framework and an adaptive numerical method for fluid–structure interaction with rigid, deforming, and elastic bodies. *J. Comput. Phys.* **250**, 446–476.

BONET, J. & WOOD, R. D. 1997 *Nonlinear Continuum Mechanics for Finite Element Analysis*. Cambridge University Press.

BORAZJANI, I. & SOTIROPOULOS, F. 2008 Numerical investigation of the hydrodynamics of carangiform swimming in the transitional and inertial flow regimes. *J. Expl Biol.* **211** (10), 1541–1558.

BORAZJANI, I. & SOTIROPOULOS, F. 2009 Numerical investigation of the hydrodynamics of anguilliform swimming in the transitional and inertial flow regimes. *J. Expl Biol.* **212** (4), 576–592.

BUCHHOLZ, J. H. J. & SMITS, A. J. 2006 On the evolution of the wake structure produced by a low-aspect-ratio pitching panel. *J. Fluid Mech.* **546**, 433–443.

BUCHHOLZ, J. H. J. & SMITS, A. J. 2008 The wake structure and thrust performance of a rigid low-aspect-ratio pitching panel. *J. Fluid Mech.* **603**, 331–365.

CHU, W.-S., LEE, K.-T., SONG, S.-H., HAN, M.-W., LEE, J.-Y., KIM, H.-S., KIM, M.-S., PARK, Y.-J., CHO, K.-J. & AHN, S.-H. 2012 Review of biomimetic underwater robots using smart actuators. *Intl J. Precis. Engng Manuf.* **13** (7), 1281–1292.

COLIN, S. P., COSTELLO, J. H., DABIRI, J. O., VILLANUEVA, A., BLOTTMAN, J. B., GEMMELL, B. J. & PRIYA, S. 2012 Biomimetic and live medusae reveal the mechanistic advantages of a flexible bell margin. *PloS One* **7** (11), e48909.

DEMONT, M. E. & GOSLINE, J. M. 1988 Mechanics of jet propulsion in the hydromedusan jellyfish, *Polyorchis penicillatus*. Part III. A natural resonating bell: the presence and importance of a resonant phenomenon in the locomotor structure. *J. Expl Biol.* **134** (1), 347–361.

DEN HARTOG, J. P. 1985 *Mechanical Vibrations*. Courier Corporation.

DEWEY, P. A, BOSCHITSCH, B. M, MOORED, K. W, STONE, H. A & SMITS, A. J 2013 Scaling laws for the thrust production of flexible pitching panels. *J. Fluid Mech.* **732**, 29–46.

DONG, H., MITTAL, R. & NAJJAR, F. M. 2006 Wake topology and hydrodynamic performance of low-aspect-ratio flapping foils. *J. Fluid Mech.* **566**, 309–343.

ELDREDGE, J. D., TOOMEY, J. & MEDINA, A. 2010 On the roles of chord-wise flexibility in a flapping wing with hovering kinematics. *J. Fluid Mech.* **659**, 94–115.

FALGOUT, R. D. & YANG, U. M. 2002 *Hypre*: a library of high performance preconditioners. In *Computational Science ICCS 2002* (ed. P. M. A. Sloot *et al.*), pp. 632–641. Springer.

FAUCI, L. J. & PESKIN, C. S. 1988 A computational model of aquatic animal locomotion. *J. Comput. Phys.* **77** (1), 85–108.

FISH, F. E. & BENESKI, J. T. 2014 Evolution and bio-inspired design: natural limitations. In *Biologically Inspired Design: Computational Methods and Tools* (ed. A. K. Goel *et al.*), pp. 287–312. Springer.

GREEN, M. A., ROWLEY, C. W. & SMITS, A. J. 2011 The unsteady three-dimensional wake produced by a trapezoidal pitching panel. *J. Fluid Mech.* **685**, 117–145.

GREEN, M. A. & SMITS, A. J. 2008 Effects of three-dimensionality on thrust production by a pitching panel. *J. Fluid Mech.* **615**, 211–220.

GRIFFITH, B. E. & LUO, X. 2016 Hybrid finite difference/finite element version of the immersed boundary method. *Int. J. Numer. Meth. Engng* **33**, 1–26.

HAMLET, C., FAUCI, L. J. & TYTELL, E. D. 2015 The effect of intrinsic muscular nonlinearities on the energetics of locomotion in a computational model of an anguilliform swimmer. *J. Theor. Biol.* **385**, 119–129.

HAMLET, C., SANTHANAKRISHNAN, A. & MILLER, L. A. 2011 A numerical study of the effects of bell pulsation dynamics and oral arms on the exchange currents generated by the upside-down jellyfish *Cassiopea xamachana*. *J. Expl Biol.* **214** (11), 1911–1921.

HERSCHLAG, G. & MILLER, L. 2011 Reynolds number limits for jet propulsion: a numerical study of simplified jellyfish. *J. Theor. Biol.* **285** (1), 84–95.

HOOVER, A. & MILLER, L. 2015 A numerical study of the benefits of driving jellyfish bells at their natural frequency. *J. Theor. Biol.* **374**, 13–25.

HOOVER, A. P., GRIFFITH, B. E. & MILLER, L. A 2017 Quantifying performance in the medusan mechanospace with an actively swimming three-dimensional jellyfish model. *J. Fluid Mech.* **813**, 1112–1155.

HORNUNG, R. D., WISSINK, A. M. & KOHN, S. R. 2006 Managing complex data and geometry in parallel structured AMR applications. *Engng Comput.* **22** (3–4), 181–195.

HOVER, F. S., HAUGSDAL, Ø. & TRIANTAFYLLOU, M. S. 2004 Effect of angle of attack profiles in flapping foil propulsion. *J. Fluids Struct.* **19** (1), 37–47.

HYPRE 2011 *Hypre*: high performance preconditioners. http://www.llnl.gov/CASC/hypre.

IBAMR 2014 IBAMR: An adaptive and distributed-memory parallel implementation of the immersed boundary method. http://ibamr.googlecode.com/.

JONES, S. K., LAURENZA, R., HEDRICK, T. L., GRIFFITH, B. E. & MILLER, L. A. 2015 Lift vs. drag based mechanisms for vertical force production in the smallest flying insects. *J. Theor. Biol.* **384**, 105–120.

KIRK, B. S., PETERSON, J. W., STOGNER, R. H. & CAREY, G. F. 2006 `libMesh`: a C++ library for parallel adaptive mesh refinement/coarsening simulations. *Engng Comput.* **22** (3–4), 237–254.

LEFTWICH, M. C., TYTELL, E. D., COHEN, A. H. & SMITS, A. J. 2012 Wake structures behind a swimming robotic lamprey with a passively flexible tail. *J. Expl Biol.* **215** (3), 416–425.

LEHN, A. M., THORNYCROFT, P. J., LAUDER, G. V. & LEFTWICH, M. C. 2017 Effect of input perturbation on the performance and wake dynamics of aquatic propulsion in heaving flexible foils. *Phys. Rev. Fluids* **2** (2), 023101.

LICHT, S. C., WIBAWA, M. S., HOVER, F. S. & TRIANTAFYLLOU, M. S. 2010 In-line motion causes high thrust and efficiency in flapping foils that use power downstroke. *J. Expl Biol.* **213** (1), 63–71.

LIU, P. & BOSE, N. 1997 Propulsive performance from oscillating propulsors with spanwise flexibility. *Proc. R. Soc. Lond.* A **453**, 1763–1770.

LUCAS, K. N., JOHNSON, N., BEAULIEU, W. T., CATHCART, E., TIRRELL, G., COLIN, S. P., GEMMELL, B. J., DABIRI, J. O. & COSTELLO, J. H. 2014 Bending rules for animal propulsion. *Nat. Commun.* **5**, 3293.

LUCAS, K. N., THORNYCROFT, P. J., GEMMELL, B. J., COLIN, S. P., COSTELLO, J. H. & LAUDER, G. V. 2015 Effects of non-uniform stiffness on the swimming performance of a passively-flexing, fish-like foil model. *Bioinspir. Biomim.* **10** (5), 056019.

MEGILL, W. M., GOSLINE, J. M. & BLAKE, R. W. 2005 The modulus of elasticity of fibrillin-containing elastic fibres in the mesoglea of the hydromedusa *Polyorchis penicillatus*. *J. Expl Biol.* **208** (20), 3819–3834.

MICHELIN, S. & LLEWELLYN SMITH, S. G. 2009 Resonance and propulsion performance of a heaving flexible wing. *Phys. Fluids* **21** (7), 071902.

MILLER, L. A. & PESKIN, C. S. 2004 When vortices stick: an aerodynamic transition in tiny insect flight. *J. Expl Biol.* **207** (17), 3073–3088.

MILLER, L. A. & PESKIN, C. S. 2005 A computational fluid dynamics of 'clap and fling' in the smallest insects. *J. Expl Biol.* **208** (2), 195–212.

MILLER, L. A. & PESKIN, C. S. 2009 Flexible clap and fling in tiny insect flight. *J. Expl Biol.* **212** (19), 3076–3090.

MITTAL, R. & IACCARINO, G. 2005 Immersed boundary methods. *Annu. Rev. Fluid Mech.* **37**, 239–261.

MOORE, M. N. J. 2014 Analytical results on the role of flexibility in flapping propulsion. *J. Fluid Mech.* **757**, 599–612.

MOORE, M. N. J. 2015 Torsional spring is the optimal flexibility arrangement for thrust production of a flapping wing. *Phys. Fluids* **27** (9), 091701.

MOORE, M. N. J. 2017 A fast Chebyshev method for simulating flexible-wing propulsion. *J. Comput. Phys.* **345**, 792–817.

PARAZ, F., ELOY, C. & SCHOUVEILER, L. 2014 Experimental study of the response of a flexible plate to a harmonic forcing in a flow. *C. R. Méc.* **342** (9), 532–538.

PESKIN, C. S. 1977 Numerical analysis of blood flow in the heart. *J. Comput. Phys.* **25** (3), 220–252.

PESKIN, C. S. 2002 The immersed boundary method. In *Acta Numerica* (ed. A. Iserles), vol. 11, pp. 479–517. Cambridge University Press.

PIÑEIRUA, M., THIRIA, B. & GODOY-DIANA, R. 2017 Modelling of an actuated elastic swimmer. *J. Fluid Mech.* **829**, 731–750.

QUINN, D. B., LAUDER, G. V. & SMITS, A. J. 2014*a* Flexible propulsors in ground effect. *Bioinspir. Biomim.* **9** (3), 036008.

QUINN, D. B., LAUDER, G. V. & SMITS, A. J. 2014*b* Scaling the propulsive performance of heaving flexible panels. *J. Fluid Mech.* **738**, 250–267.

QUINN, D. B., LAUDER, G. V. & SMITS, A. J. 2015 Maximizing the efficiency of a flexible propulsor using experimental optimization. *J. Fluid Mech.* **767**, 430–448.

RAJ, A. & THAKUR, A. 2016 Fish-inspired robots: design, sensing, actuation, and autonomy. A review of research. *Bioinspir. Biomim.* **11** (3), 031001.

RAMANANARIVO, S., GODOY-DIANA, R. & THIRIA, B. 2011 Rather than resonance, flapping wing flyers may play on aerodynamics to improve performance. *Proc. Natl Acad. Sci.* **108** (15), 5964–5969.

RICHARDS, A. J. & OSHKAI, P. 2015 Effect of the stiffness, inertia and oscillation kinematics on the thrust generation and efficiency of an oscillating-foil propulsion system. *J. Fluids Struct.* **57**, 357–374.

ROOT, R. G. & COURTLAND, H.-W. 1999 Swimming fish and fish-like models: the harmonic structure of undulatory waves suggests that fish actively tune their bodies. In *International Symposium on Unmanned Untethered Submersible Technology*, pp. 378–388. University of New Hampshire, Marine Systems.

SAMRAI 2007 SAMRAI: Structured Adaptive Mesh Refinement Application Infrastructure http://www.llnl.gov/CASC/SAMRAI.

SHOELE, K. & ZHU, Q. 2012 Leading edge strengthening and the propulsion performance of flexible ray fins. *J. Fluid Mech.* **693**, 402–432.

DE SOUSA, P. J. F. & ALLEN, J. J. 2011 Thrust efficiency of harmonically oscillating flexible flat plates. *J. Fluid Mech.* **674**, 43–66.

SPAGNOLIE, S. E., MORET, L., SHELLEY, M. J. & ZHANG, J. 2010 Surprising behaviors in flapping locomotion with passive pitching. *Phys. Fluids* **22** (4), 041903.

TAYLOR, G. K., NUDDS, R. L. & THOMAS, A. L. 2003 Flying and swimming animals cruise at a Strouhal number tuned for high power efficiency. *Nature* **425** (6959), 707–711.

TRIANTAFYLLOU, G. S., TRIANTAFYLLOU, M. S. & GROSENBAUGH, M. A. 1993 Optimal thrust development in oscillating foils with application to fish propulsion. *J. Fluids Struct.* **7**, 205–224.

TYTELL, E. D., HSU, C.-Y. & FAUCI, L. J. 2014 The role of mechanical resonance in the neural control of swimming in fishes. *Zoology* **117** (1), 48–56.

TYTELL, E. D., HSU, C.-Y., WILLIAMS, T. L., COHEN, A. H. & FAUCI, L. J. 2010 Interactions between internal forces, body stiffness, and fluid environment in a neuromechanical model of lamprey swimming. *Proc. Natl Acad. Sci.* **107** (46), 19832–19837.

TYTELL, E. D., LEFTWICH, M. C., HSU, C.-Y., GRIFFITH, B. E., COHEN, A. H., SMITS, A. J., HAMLET, C. & FAUCI, L. J. 2016 Role of body stiffness in undulatory swimming: insights from robotic and computational models. *Phys. Rev. Fluids* **1** (7), 073202.

VAN BUREN, T., FLORYAN, D., BRUNNER, D., SENTURK, U. & SMITS, A. J. 2017 Impact of trailing edge shape on the wake and propulsive performance of pitching panels. *Phys. Rev. Fluids* **2** (1), 014702.

VAN BUREN, T., FLORYAN, D., WEI, N. & SMITS, A. J. 2018 Flow speed has little impact on propulsive characteristics of oscillating foils. *Phys. Rev. Fluids* **3**, 013103.

VAN EYSDEN, C. A. & SADER, J. E. 2006 Resonant frequencies of a rectangular cantilever beam immersed in a fluid. *J. Appl. Phys.* **100** (11), 114916.

VAN EYSDEN, C. A. & SADER, J. E. 2007 Frequency response of cantilever beams immersed in viscous fluids with applications to the atomic force microscope: arbitrary mode order. *J. Appl. Phys.* **101** (4), 044908.

VAN EYSDEN, C. A. & SADER, J. E. 2009 Frequency response of cantilever beams immersed in compressible fluids with applications to the atomic force microscope. *J. Appl. Phys.* **106** (9), 094904.

VANDENBERGHE, N., CHILDRESS, S. & ZHANG, J. 2006 On unidirectional flight of a free flapping wing. *Phys. Fluids* **18** (1), 014102.

WEAVER, W., TIMOSHENKO, S. P. & YOUNG, D. H. 1990 *Vibration Problems in Engineering*. Wiley.

WILLIAMSON, C. H. K. & ROSHKO, A. 1988 Vortex formation in the wake of an oscillating cylinder. *J. Fluids Struct.* **2** (4), 355–381.

YEH, P. D. & ALEXEEV, A. 2014 Free swimming of an elastic plate plunging at low Reynolds number. *Phys. Fluids* **26** (5), 053604.

ZHANG, C., GUY, R. D., MULLONEY, B., ZHANG, Q. & LEWIS, T. J. 2014 Neural mechanism of optimal limb coordination in crustacean swimming. *Proc. Natl Acad. Sci. USA* **111** (38), 13840–13845.

ZHU, X., HE, G. & ZHANG, X. 2014 Numerical study on hydrodynamic effect of flexibility in a self-propelled plunging foil. *Comput. Fluids* **97**, 1–20.